**INSTITUT FÜR
ENERGIETECHNIK
UND THERMODYNAMIK**
Institute of Energy Systems and Thermodynamics

Master's Thesis

Simulation of industrial droplet separators

under the supervision of

Assistant Prof. Dipl.-Ing. Bernhard Semlitsch, PhD

E302 - Institute of Energy Systems and Thermodynamics

submitted to the Faculty of Mechanical and Industrial Engineering
of Technische Universität Wien
for the degree of Master of Science (MSc.)

by

Ján Dudaško, BSc
Matr.Nr. 01425878

Wien, April 2024

....
(Ján Dudaško, BSc)

Statutory Declaration

This thesis is the result of my own work and includes nothing that is the outcome of work done in collaboration except as specified in the text.

It is not substantially the same as any that I have submitted, or, is being concurrently submitted for a degree or diploma or other qualification at Technische Universität Wien or any other University or similar institution except as specified in the text. I further state that no substantial part of my thesis has already been submitted, or, is being concurrently submitted for any such degree, diploma or other qualification at Technische Universität Wien or any other University or similar institution except as specified in the text.

Wien, April 2024

(Ján Dudaško, BSc)

Acknowledgements

I would like to thank my supervisor, Assistant Prof. Dipl.-Ing. Bernhard Semlitsch, PhD for his expertise and friendly support throughout the the whole thesis.

Furthermore, I want to express my gratitude to my parents for making my studies possible and for supporting me unconditionally throughout the years.

Last, but not least, a huge thank you to my girlfriend Miriam for always believing in me and supporting me on every level.

Abstract

Many chemical processes utilise droplet separators. Droplet separators can be constructed in several ways, utilising different physical phenomena. Correct design and operation of these components play a vital role in the overall process efficiency. Their reliable functionality under all operating conditions is therefore of immense importance.

A common way to investigate the flow conditions inside droplet separators is the use of computational fluid dynamic simulations. The steady-state simulations are performed using ANSYS® FLUENT®. The water-vapour flow field is predicted as a continuous phase in the Eulerian reference frame and water droplets are injected utilising the Lagrangian reference frame in the form of the discrete particle model. Water separation on the walls is realised via the coupling of the discrete particle model with the Eulerian wall film model. Turbulence is solved using the k-ω SST turbulence model.

Three industrial cyclone separator geometries are investigated. The internal length scales of industrial droplet separators can reach several meters. This poses a challenge due to the necessity of sufficient mesh resolution to resolve the water droplet adherence in the entire geometry. The meshing process in ANSYS® FLUENT® requires significant computational resources with the need for a graphical interface. The numerical simulations as well as pre- and post-processing were performed on the Vienna Scientific Cluster. The computed flow fields are analysed and the efficiency of the investigated separator geometries is evaluated and compared considering varying total droplet mass and droplet diameter distributions.

Kurzfassung

Tröpfchenabscheider werden in vielen chemischen Prozessen eingesetzt. Sie können in unterschiedlichen Bauformen ausgeführt werden, wobei die für ihre Funktionsweise relevante physikalische Phänomene auch diskrepant sein können. Die richtige Konstruktion und der korrekte Betrieb dieser Komponenten spielen eine entscheidende Rolle für die Effizienz des gesamten Prozesses. Die zuverlässige Funktionalität unter allen Betriebsbedingungen ist daher von immenser Bedeutung.

Die Untersuchung der Strömungsverhältnisse in einem Tröpfchenabscheider erfolgt in der Praxis häufig durch numerische Strömungssimulationen. Die Berechnungen werden als stationäre Simulationen mithilfe von ANSYS® FLUENT®. Das Strömungsfeld wird in Euler'schen Betrachtungsweise vorhergesagt, wobei der Wasserdampf als kontinuierliche Phase angenommen wird. Die Wassertröpfchen werden in Lagrange'schen Betrachtungsweise mit Hilfe des Discrete-Particle-Modells eingeleitet. Die Wasserabscheidung an den Wänden wird durch die Kopplung des Discrete-Particle-Modells mit dem Eulerschen Wandfilmmodell realisiert. Als Turbulenzmodell wird SST k-ω eingesetzt.

Drei industrierelevante Zyklonabscheidergeometrien werden untersucht. Die internen Abmessungen von solchen Tröpfchenabscheidern können mehrere Meter betragen. Dies stellt eine Herausforderung dar, da eine ausreichende Meshauflösung erforderlich ist. Die Mesherstellung mit ANSYS® FLUENT® erfordert signifikante Rechenressourcen mit der Möglichkeit einer grafischen Benutzeroberfläche. Die numerischen Simulationen sowie das Pre- und Post-Processing werden auf dem Vienna Scientific Cluster durchgeführt. Die berechneten Strömungsfelder werden analysiert und die Effizienz der untersuchten Bauformen wird unter Berücksichtigung variierender Tröpfchengesamtmasse und Tröpfchendurchmesserverteilungen evaluiert und gegenübergestellt.

Contents

Contents

Contents

Nomenclature

Abbrevations

CAD	Computer-aided design
CFD	Computational fluid dynamics
DNS	Direct numerical simulation
DPM	Discrete phase model
EWFM	Eulerian wall film model
GB	Gigabyte
GHz	Gigahertz
LES	Large eddy simulation
RAM	Random access memory
RANS	Raynolds-averaged Navier-Stokes simulations
RNG	Renormalization group
SIMPLEC	Semi-Implicit Method for Pressure Linked Equations-Consistent
SST	Shear-stress transport
VoF	Volume of fluid
VSC	Vienna Scientific Cluster

Physical Constants

g	Gravitational acceleration	m/s^2

Latin Symbols

$\dot{m}$	Mass flow rate	kg/s
E	Energy	kg m^2/s^2
F	Mass flux	kg/(m^2 s)
k	Turbulent kinetic energy	m^2/s^2
L	Characteristic length	m
n	Material uniformity constant	1

p	Static pressure	Pa
r_d	Droplet diameter	m
Re	Reynolds number	1
S_j	Source term for arbitrary quantity j	
t	Time	s
u	Velocity	m/s
x	Spatial direction	1
Y	Cumulative mass fraction	1
y^+	Dimensionless wall distance	1

Greek Symbols

α	Volume fraction	1
α'	Turbulence dampening factor	1
ℓ	Particle diameter	m
ℓ_0	Characteristic particle size	m
ϵ	Rate of dissipation of turbulent kinetic energy	m^2/s^3
Γ	Diffusion coefficient	1
μ	Dynamic viscosity	Pa s
μ_m	Molecular viscosity	Pa s
μ_t	Turbulent viscosity	Pa s
ν	Kinematic viscosity	m^2/s
ω	Specific rate of dissipation of the turbulence kinetic energy	1/s
ρ	Density	kg/m^3
σ	Turbulent Prandtl number	1
τ	Wall shear stress	Pa

Vectors and Tensors

$\overline{\overline{\tau}}$	Stress tensor	
$\vec{F}$	Vector of external body forces	
$\vec{u}$	Velocity vector	
I	Unit tensor	

Chapter 1

Introduction

1.1 Motivation

This thesis shall evaluate the functionality and efficiency of an industrial droplet separator employing computational fluid dynamic methods. Droplet separators are essential in the chemical process chain. If not functioning correctly, the downstream elements can be damaged and precautionary maintenance would be enforced. The resulting production and economic losses highlight the importance of the droplet separators.

The investigated droplet separator is operating at the production site of an industry partner. Its expected efficiency levels have not been met. To understand the reasons for not reaching the efficiency targets, the flow inside the droplet simulator is to be simulated numerically. Based on the results, improvements can be proposed and tested. The improvements should increase the efficiency level while also considering aspects of technical realisability.

1.2 Scope of work

The main goals of the thesis are to determine the current functionality of the droplet separator and to investigate possible adaptations and their influence on separation efficiency. Therefore, this thesis focuses on the following main research questions:

- What are the relevant characteristics of the flow field inside a droplet separator?

- How do they influence the droplet separation efficiency?

- To what extent can they be adjusted by simple changes to the droplet separator geometry?

This thesis shall cover the following main goals:

1. Literature research

   (a) Study the theory of droplet separators

   (b) Investigate the relevant simulation strategies

2. Numerical simulation

   (a) Implement and test the chosen methodology

   (b) Reproduce the flow conditions of the installed droplet separator

   (c) Evaluate the droplet separation efficiency

3. Adaptations

   (a) Propose adaptations

   (b) Evaluate the flow field and the droplet separation efficiency of the adapted variants

Chapter 2

Theory of vapour-liquid separation

This chapter reviews the theoretical background of the basic relevant physical aspects of gas-liquid mixtures as well as the commonly used droplet separators.

2.1   Gas-liquid mixture

Many engineering problems as well as natural fluid flows consist of a mixture of substances in different states. Generally, the nature of the multi-phase system and hence the multi-phase flow need to be considered when such problems are investigated. The most common types of multi-phase flow consist of two phases of some substances. When studying the mixture of liquid and gas, the resultant flow field depends on the relative amount of liquid and gas. [40]

2.1.1   Flow regimes

Gas-liquid flows are the most complex out of the four possible two-phase flows (gas-liquid, gas-solid, liquid-liquid, and liquid-solid) due to the deformability and compressibility of the interface [20]. There are five basic types of interface distributions in gas-liquid flows, in the literature known as flow regimes, usually illustrated as a basic tube flow, which is shown in Fig.2.1 [20, 21]. The flow topologies are ordered with increasing proportion of gas in the control volume:

1. Bubble flow: As the name suggests, the liquid builds the continuous phase,

and the gas is dispersed in the form of bubbles throughout the flow.

2. Slug flow: The bubbles coalesce and their diameter nears that of the tube itself.

3. Churn flow: The slug flow bubbles break down and begin to oscillate, forming a chaotic flow.

4. Wispy annular flow: With increasing gas flow rate, the gas becomes the continuous phase with liquid film on the walls. The liquid droplets of relatively large dimensions are dispersed in the volume and the wall film contains gas bubbles.

5. Annular flow: Here, similarly to a wispy annular regime, the gas represents the continuous phase and the liquid builds a film on the walls. The droplets do not coalesce to form larger drops.
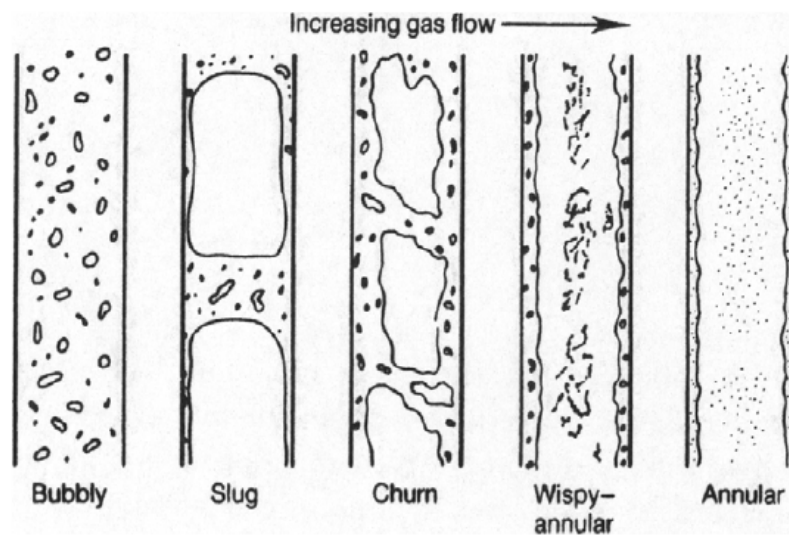
Figure 2.1: Flow regimes of a two-phase gas-liquid flow in a vertical tube. [21]

2.1.2 Droplet size

In most cases, droplets of many different sizes will coexist at the same time. Basic classification separates mists and sprays in regards to droplet size, where mists are characterised by droplet diameters of less than 10 μm, and mixtures containing

larger droplets are described as sprays [7]. In both cases, a distribution function is often used to describe the characteristics. There are many usable distribution functions, without a particular correct one. In most cases, it is common to fit experimental data to a distribution function [48]. In that case, the Rosin-Rammler [3, 54] distribution (Eq.2.1) has become the defacto standard choice.

$$Y = 1 - exp(-\ell/\ell_0)^n \qquad (2.1)$$

with Y being the cumulative fraction of material by weight less than size ℓ, n the uniformity constant of the given material and ℓ_0 the characteristic particle size, defined as the size, at which 63.2% (by weight) are smaller [54]. Fig. 2.2 shows a typical Rosin-Rammler distribution in integral form.
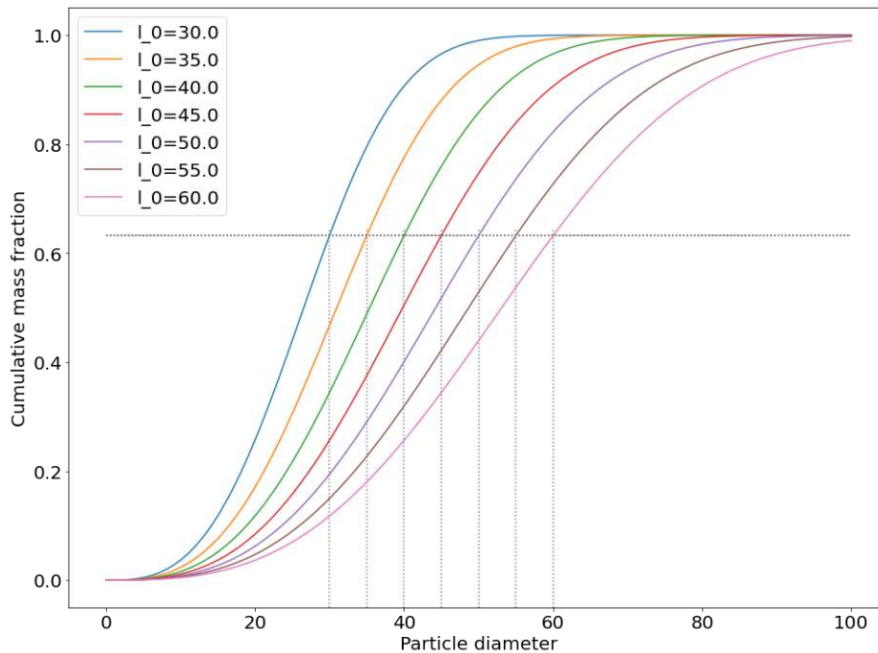
Figure 2.2: Plot of a typical cumulative Rosin-Rammler distribution according to Eq.2.1. The distribution shows 7 characteristic particle sizes ranging from 30 to 60 in diameter (arbitrary unit) with the uniformity constant of 3. The horizontal dotted line denotes the 63.2%, the vertical dotted lines reflect the characteristic particle sizes ℓ_0.

Alternatively, an average droplet diameter d_{nm} can be calculated to represent the spray. One example would be the Sauter mean diameter, which is proportional to the ratio of the total liquid volume in the spray to the total droplet surface area in

the spray [48]. Detailed publications on the droplet physics can be found in [5].

2.2 Droplet separators

Every fluid dynamic process containing gaseous and liquid phase contact under favourable conditions generates a mixing effect, where liquid droplets are carried away with the gas flow. This mixing generally results in efficiency losses of droplet separators in downstream industrial processes and can damage the equipment [14]. The choice of a correct droplet separator for the application in question is therefore of immense importance.

2.2.1 Scope of application

Droplet separators are widely used as a process-optimising component. Common applications are [39], [58]:

1. reduction of material losses in other components (absorbers, evaporators, distillation columns),

2. increased product quality in distillation columns due to lower contamination,

3. corrosion reduction in downstream components, and

4. protection of rotating equipment (compressors and pumps).

2.2.2 Physical principle

All droplet separators work based on the principle of balance manipulation of acting forces on the multiphase flow medium. There are several fundamental mechanisms how to separate the phases, which distinguish the basic separator types discussed

below. Analytical investigations describe the acting forces as follows[25]:

$$
\rho_d \frac{d\vec{u}_d}{dt} - \rho_g \frac{D\vec{u}_{gd}}{Dt} = (\rho_d - \rho_g)\,\vec{g} + \frac{1}{\rho_g}\left[\left(\frac{d\vec{u}_{gd}}{dt} - \frac{d\vec{u}_d}{dt}\right) + \frac{1}{10}r_d^2\frac{d\nabla^2\vec{u}_{gd}}{dt}\right]
$$
$$
- \frac{9\mu_g}{2r_d^2}\left(\vec{u}_d - \vec{u}_{gd} - \frac{1}{6}r_d^2\nabla^2\vec{u}_{gd}\right) - \frac{9\mu_g}{2r_d}\int_0^t d\tau\,\frac{\frac{d}{d\tau}\left(\vec{u}_d - \vec{u}_{gd} - \frac{1}{6}r_d^2\nabla^2\vec{u}_{gd}\right)}{\sqrt{\pi u_g(t-\tau)}}
$$
$$
+ 4.845\frac{\mu_g}{\pi r_d}\sqrt{\frac{1}{u_g}\left|\frac{du_g}{dy}\right|}\,(\vec{u}_d - \vec{u}_g) \quad (2.2)
$$

where the indices g and d represent gas and droplet, respectively, and $\vec{u_{gd}}$ is the undisturbed velocity at the droplet centre. r_d is the droplet diameter, d/dt the time derivative following the moving droplet, and D/Dt is the time derivative using the undisturbed gas velocity as the convective velocity [25]. The terms on the right-hand side (in the same order as in Eq.2.2) refer to:

1. gravity or buoyancy

2. virtual mass

3. drag force

4. history

5. lift force with y being the vertical direction.

Additionally, there is the pressure force and Magnus force which are usually neglected. Pressure forces result from the pressure gradient driving the flow. The droplet diameters are too small to experience any relevant pressure gradient. The Magnus force is present for all rotating bodies but the magnitude is too low to have any real influence [25].

2.2.3 Types of droplet separators

The following description makes no claim to be complete but intends to provide an overview of the most commonly used separators. More details can be found in [7].

Impingement separators

The droplets interact with a surface inside the separator (target). The ability of the droplet to hit the target increases with gas velocity and particle weight. As soon as the droplet comes into contact with the target, it adheres to the surface by weak Van Der Waals forces [58].

There are three different mechanisms that allow for droplet impingement [14], [58]:

1. Inertial impact: Droplets with sufficient mass have high enough momentum to deviate from the gas streamlines and thereby hitting the target directly.

2. Direct interception: Smaller droplets following the streamlines can be collected if the streamline lies sufficiently close to the target, i.e. less than half of the droplet diameter from the centre line. In that case, the droplet can touch the target and be collected.

3. Diffusion: The smallest droplets ($d < 1\mu m$) follow random Brownian motion due to collisions with gas molecules. This way, the smallest droplets can be collected even if the gas velocity is zero.

There are several versions of targets, e.g.: wire mesh, fibre beds, or baffle type units [58].

Gravity settlers

This type of separator uses a comparably large gas velocity drop in order to decrease the drag forces and therefore allowing a settlement of the droplets on the bottom of the separator. The geometry and construction are usually kept simple, typically in the form of a horizontal cylinder [6]. It can be effectively used only for large droplets (d>$250\mu m$) [9, 14]. This type of separator is fairly common in oil and gas field applications as initial step in a series of droplet separators, usually followed by an impingement separator [10, 27]. The efficiency depends greatly on the position of in- and outlets as well as the use of baffles inside the separator [46].

Electrostatic precipitators

The gas flows between two electrodes, charging any included particles. These are subsequently pulled toward the electrode with an opposite charge where they impinge and can be collected. This version is best suited for very fine particles ($d < 1\mu m$) [7].

Centrifugal separators

In a typical centrifugal separator construction, the gas flow enters the separator tangentially in the top part and is subsequently forced to follow a double vortex: a spiral downwards along the wall and only then upwards through the centre. The acting centrifugal force directs the droplets to the wall, where they impinge and get collected at the bottom of the separator. The overall form of the separator can be either conical or cylindrical [7]. The cyclone profile needs to be constructed in regards to the anticipated droplet sizes and flow characteristics in order to achieve high efficiency [16, 22, 32, 44]. The separation efficiency for a known flow can be calculated during the designing stage [34].

Investigated droplet separator

The basic principle is similar to a classical cyclone (centrifugal) separator. The main difference is the flow direction, as there is no central immersion tube, but a downpipe. The gas-fluid mixture enters through the two tangential inlets and is forced into a rotating motion along the outer wall. The separation of the fluid happens via interaction with the wall due to centrifugal force. The gas rises upwards and escapes through the centrally mounted downpipe. The fluid flows down the outer wall and exits the separator via the outlet, positioned in the lowest part. A schematic operation mode is provided in Fig.2.3a. A cross-section of the modelled geometry inclusive details (e.g. reinforcement pipes) can be seen in Fig.2.3b.
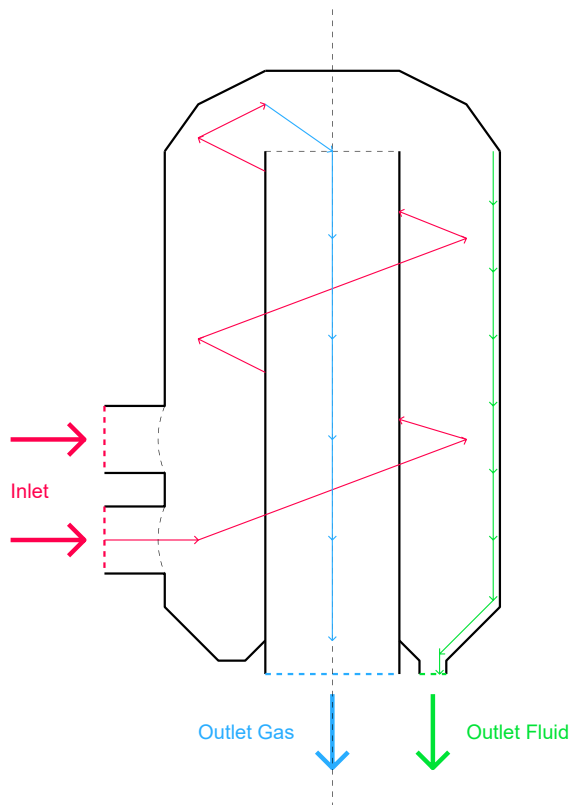
(a) Schematic sketch of the installed separator and
its function
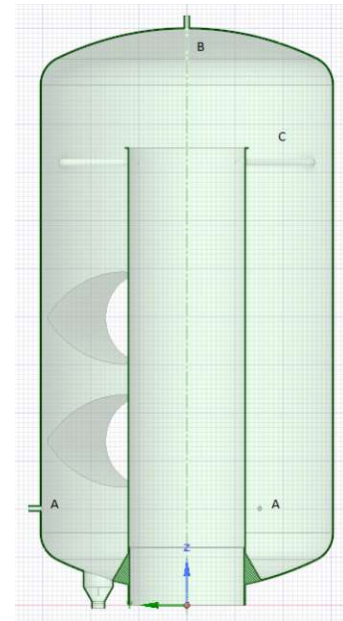
(b) Cross section of the
investigated separator,
details: A: cleaning
nozzle pass-through,
B: Reserve (unused),
C: reinforcement pipes

Figure 2.3: Geometry of the installed separator

In order to understand the role of the separator as a part of the whole process,
Fig.2.4 is provided. The product is marked via blue arrows, vapour via orange,
additional steam via red, and cooling water via green arrows. The black arrow
shows the electric energy for the compressor. The numbering complies with the
following scheme: 1: vapour compressor, 2: falling film evaporator, 3: droplet
separator, 4: condenser.
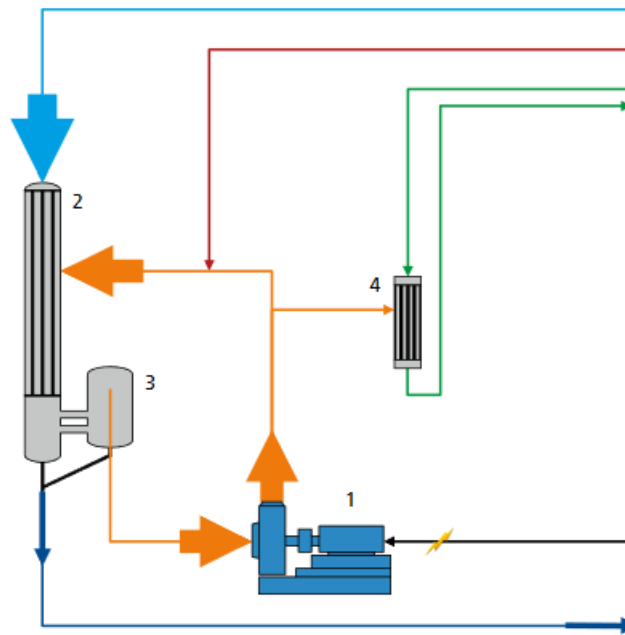
Figure 2.4: Process of evaporation with subsequent vapour-compression. The droplet separator is incorporated between the evaporator and the compressor. The figure's purpose is to only visualise the process and it does not correspond to the actual equipment on site.[19]

Chapter 3

Numerical simulation strategies

The aim of this chapter is to present the governing equations and to describe the known simulation models, as well as to choose the most appropriate one for the problem at hand. As usual in computational fluid dynamics (CFD), the calculations are performed in Eulerian description, i.e. with a fixed control volume.

3.1   Finite volume method

The finite volume method is based on the conservation of fluxes in small volume cells. The conservation laws have to be interpreted in integral form to preserve discontinuous solution [35] as vortex sheets, contact discontinuities or shock waves. The physical domain is divided into small volume cells, where the integrals are evaluated as sums over the bounding surfaces of these cells [30]. The flow field variables are calculated in some discrete points of each cell, which are interpreted as average values over the finite volumes [15]. The conservation laws are then applied to the finite volumes to obtain the discrete equations. [36, 52] The method has established itself in the area of computational fluid dynamics due to the good balance of accuracy and flexibility, as shown in Fig. 3.1.
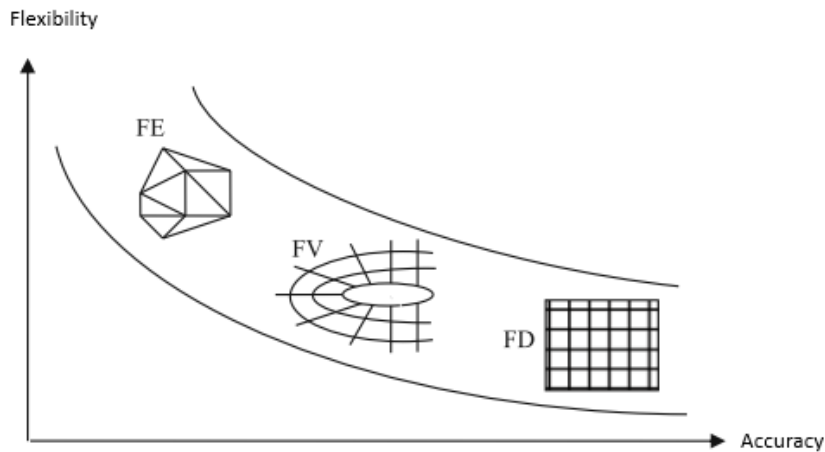
Figure 3.1: Discretisation methods and their application areas. [30]

3.2 Governing equations

The fundamental equations describing the fluid dynamic motion are the well-established Navier-Stokes equations, presented here in the Einstein-summation convention [45]:

$$\frac{\partial \left(\rho u_i \right)}{\partial t} + \frac{\partial (\rho u_i u_j)}{\partial x_j} = \rho g_i - \frac{\partial p}{\partial x_i} + \mu \nabla^2 u_i + \frac{1}{3}\mu \frac{\partial}{\partial x_i}\left(\frac{\partial u_j}{\partial x_j} \right) \tag{3.1}$$

where $i,\ j$ denote the three dimensional coordinates; x the individual directions u the velocity; ρ the density; μ the dynamic viscosity; g the gravitational acceleration; p the static pressure and t the time.

Although empirically validated, there is no known analytical solution, except for the case of simple laminar flows.

The software used in this thesis is ANSYS® FLUENT®, the equations listed below are presented in the same notation as used in the corresponding theory guide.

3.2.1 Conservation equations

The mass conservation equation [1] in its general form with S_m being the mass added to the continuous phase from the dispersed phase:

$$\frac{\partial \rho}{\partial t} + \nabla \cdot (\rho \vec{u}) = S_m \tag{3.2}$$

Conservation of momentum [1], where p is the static pressure, $\overline{\overline{\tau}}$ the stress tensor, $\vec{g}$ the gravitational acceleration, and $\vec{F}$ the external body forces:

$$\frac{\partial}{\partial t}(\rho\vec{u}) + \nabla \cdot (\rho\vec{u}\vec{u}) = -\nabla p + \nabla \cdot (\overline{\overline{\tau}}) + \rho\vec{g} + \vec{F} \tag{3.3}$$

where the stress tensor $\overline{\overline{\tau}}$ reads as:

$$\overline{\overline{\tau}} = \mu_m \left[\left(\nabla\vec{u} + \nabla\vec{u}^T \right) - \frac{2}{3}\nabla \cdot \vec{u}I \right] \tag{3.4}$$

with μ_m being the molecular viscosity and I the unit tensor.

3.2.2 Transport equation

The multiphase transport equation [1], which distinguishes between scalars per phase and for the whole mixture can be written for an arbitrary k-scalar denoted by ϕ_l^k as:

$$\frac{\partial \alpha_l \rho_l \phi_l^k}{\partial t} + \nabla \cdot \left(\alpha_l \rho_l \vec{u}_l \phi_l^k - \alpha_l \Gamma_l^k \nabla \phi_l^k \right) = S_l^k \quad \text{where} \quad k = 1, \ldots, N . \tag{3.5}$$

The meaning of the symbols is as follows: α_l represents the volume fraction, ρ_l the physical density and $\vec{u}_l$ the velocity. Γ_l^k is the diffusion coefficient and S_l^k the source term which needs to be specified. The subscript l means phase l.

The mass flux for phase l through a control volume is defined as:

$$F_l = \int_S \alpha_l \rho_l \vec{u}_l \cdot d\vec{S} . \tag{3.6}$$

If the variable described by the scalar ϕ_l^k is shared between phases or is considered the same for all phases, the transport equation for the mixture needs to be used:

$$\frac{\partial \rho_m \phi^k}{\partial t} + \nabla \cdot \left(\rho_m \vec{u_m} \phi^k - \Gamma_m^k \nabla \phi^k \right) = S^{k_m} \quad \text{where} \quad k = 1, \ldots, N . \tag{3.7}$$

The involved quantities are the mixture density ρ_m, mixture velocity $\vec{u_m}$, mixture

diffusivity Γ_m^k and the source term S_m^k are calculated as follows:

$$\rho_m = \sum_l \alpha_l \rho_l \tag{3.8}$$

$$\rho_m \vec{u_m} = \sum_l \alpha_l \rho_l \vec{u_l} \tag{3.9}$$

$$\Gamma_m^k = \sum_l \alpha_l \Gamma_l^k \tag{3.10}$$

$$S_m^k = \sum_l S_l^k \tag{3.11}$$

The mass flux for a mixture needs to be also constructed accordingly:

$$F_m = \int_S \rho_m \vec{u_m} \cdot d\vec{S} \tag{3.12}$$

3.3 Turbulence models

Fluid flows can be categorised into basic groups: laminar and turbulent flows. In the case of laminar flows, the fluid elements follow parallel trajectories without small-scale vortexes. Turbulence on the other hand, is always three-dimensional and unsteady in time and space. The flow can be characterised by the Reynolds number,

$$Re = \frac{u \cdot L}{\nu} \ , \tag{3.13}$$

where u denotes the fluid velocity, L is the characteristic length, and ν is the kinematic viscosity of the fluid. There is a critical Reynolds number for each flow type, above which the flow switches from laminar to turbulent. Almost every engineering-relevant flow operates at least partially within the turbulent regime. Due to the random nature of turbulence, no deterministic solution approach is possible. Statistical methods allow for certain correlations within the flow, although these are strongly dependent on the upstream history and cannot be classified regarding their local occurrence. To perform a CFD simulation of a turbulent flow, one needs a suitable approach. Three main categories, Direct numerical simulation (DNS), Large eddy simulation (LES) and Raynolds-averaged Navier-Stokes (RANS) are broadly accepted and used. There are also recently developed hybrid models, which combine the three methods, although still only for very specific cases [56].

3.3.1 Direct Numerical Simulation

In order to perform a Direct Numerical Simulation (DNS) of a turbulent flow, all dynamically relevant scales need to be resolved on the numerical grid down to Kolmogorov microscale [29]. The computational domain must be at least an order of magnitude larger than the scales characterising the turbulence energy [57]. The resulting need for computational resources rises approximately with $Re^{9/4}$ [29]. Due to these reasons, the DNS can only be efficiently performed for small geometries and low Reynolds numbers [53]. Using contemporary computational equipment, DNS for applications on an industrial scale remain impossible [29, 38]. DNS in combination with machine learning might become a useful tool in the future [17].

3.3.2 Large Eddy Simulation

As the name Large Eddy Simulation (LES) suggests, the method simulates, in contrary to DNS, only some of the turbulent flow scales. Large-scale motions (large eddies) are computed, whereas the small ones, which tend to be more isotropic and homogeneous, are modelled [18]. Thereby, the motions containing the most turbulent energy and being responsible for the most momentum transfer and turbulent mixing are computed accurately. The difference to DNS occurs at the level of small eddies, which are not resolved on the utilised grid and are modelled instead. A low-pass spatial filter is needed to filter the governing Navier-Stokes equations. The filter can be either in Fourier space or in physical space. It filters out the eddies, which are smaller than the grid spacing or the filter width [31]. Effectively, what remains are the governing equations for the dynamics of the large eddies [1]. If the filter boundary is pushed to the extremely low side, the resulting simulation effectively becomes a DNS. Although this approach provides higher accuracy than RANS at lower costs than DNS, the involved computational costs are still too high for most industrial applications [57]. The literature stipulates that LES will become the industry standard in the future, provided the computational power continues to rise [57]. The droplet separator that is to be simulated in this thesis does not allow for a feasible LES due to it's size.

3.3.3 Raynolds-Averaged Navier-Stokes simulations

In case of Raynolds-Averaged Navier-Stokes (RANS) simulations, the basis of the model is a decomposition of the flow properties into average and fluctuation values [11, 13]. The decomposition can be written as:

$$u_i = \overline{u_i} + u_i'$$

where $\overline{u_i}$ denotes the average velocity, u_i' is the fluctuating part of the velocity, and $i = 1, 2, 3$ assigns the velocity component to a spatial coordinate. The time-average of the fluctuations is per definition zero. The statistical details of the fluctuation quantities are commonly not available. The same decomposition is valid also for pressure and other scalar quantities. The goal of this approach is to introduce equations for the averaged properties, while the velocity fluctuation components need to be modelled or determined by transport equations. Thereby, the RANS equations can be stated in Cartesian form. These represent the continuity (3.14) and momentum (3.15) equation (which have been time-averaged and the overbar over the mean velocity has been dropped) [1]:

$$\frac{\partial \rho}{\partial t} + \frac{\partial}{\partial x_i}\left(\rho u_i\right) = 0 \tag{3.14}$$

$$\begin{aligned}
\frac{\partial}{\partial t}\left(\rho u_i\right) + \frac{\partial}{\partial x_j}\left(\rho u_i u_j\right) = {}&-\frac{\partial p}{\partial x_i} + \frac{\partial}{\partial x_j}\left[\mu\left(\frac{\partial u_i}{\partial x_j} + \frac{\partial u_j}{\partial x_i} - \frac{2}{3}\delta_{ij}\frac{\partial u_i}{\partial x_i}\right)\right] \\
&+ \frac{\partial}{\partial x_j}\left(-\rho\overline{u_i' u_j'}\right) \ .
\end{aligned} \tag{3.15}$$

The last term of the Eq. 3.15 is the so-called Raynolds stress, which must be modelled in order to close the equation system. Therefore, the Boussinesq hypothesis (3.16) is widely used, which relates the Reynolds stresses to the mean velocity gradients [1]:

$$-\rho\overline{u_i' u_j'} = \mu_t\left(\frac{\partial u_i}{\partial x_j} + \frac{\partial u_j}{\partial x_i}\right) - \frac{2}{3}\left(\rho k + \mu_t\frac{\partial u_k}{\partial x_k}\right)\delta_{ij} \tag{3.16}$$

μ_t denotes the turbulent viscosity and k the turbulent kinetic energy. There are several closure models for the Reynolds stress problem, which are based on the Boussinesq hypothesis, e.g. $k - \omega$ or $k - \epsilon$. These will be discussed in detail below.

3.4 RANS Closure models

In this section, a description of the known turbulence closure models will be provided, as well as their respective strengths and weaknesses. In the end, an appropriate turbulence model is chosen. Over the years, many different models have been developed. Table 3.1 shows an overview of the most commonly used closure models and their main attributes.

The $k - \epsilon$ and $k - \omega$ models are most relevant for engineering practice. Therefore, a more detailed description of these two models including the respective equations is provided.

3.4.1 $k - \epsilon$

The standard $k - \epsilon$ model is most commonly employed two-equation turbulence model, which means that it allows for determination of the turbulent length and time scale by solving two separate transport equations [28]. The model is based on transport equations for the turbulence kinetic energy (k) and its dissipation rate (ϵ). This model is valid only for fully turbulent flows and the effects of molecular viscosity need to be negligible. The $k - \epsilon$ model does not succeed in reproducing flows which separate from the walls due to adverse pressure gradients [30]. The separation is detected too late and the size of the separation area is commonly underestimated. The transport equations are [1]:

$$\frac{\partial}{\partial t}(\rho k) + \frac{\partial}{\partial x_i}(\rho k u_i) = \frac{\partial}{\partial x_j}\left[\left(\mu + \frac{\mu_t}{\sigma_k}\right)\frac{\partial k}{\partial x_j}\right] + G_k + G_b - \rho\epsilon - Y_M + S_k \quad (3.17)$$

and

$$\frac{\partial}{\partial t}(\rho\epsilon) + \frac{\partial}{\partial x_i}(\rho\epsilon u_i) = \frac{\partial}{\partial x_j}\left[\left(\mu + \frac{\mu_t}{\sigma_\epsilon}\right)\frac{\partial\epsilon}{\partial x_j}\right] + C_{1\epsilon}\frac{\epsilon}{k}(G_k + C_{3\epsilon}G_b) - C_{2\epsilon}\rho\frac{\epsilon^2}{k} + S_\epsilon$$

$$(3.18)$$

with the following quantities:

- G_k: generation of turbulence kinetic energy due to the mean velocity gradients

- G_b: generation of turbulence kinetic energy due to buoyancy

- Y_M: contribution of the fluctuating dilatation in compressible turbulence to

Model	Description	Behaviour
Spalart-Almaras	- one equation model - designed for aerospace applications - for wall-bounded flows on a fine near-wall mesh	- poor performance in 3D / free shear flows / flows with strong separation - economical for large meshes
Standard $k - \epsilon$	- two equation model - valid for fully turbulent floes only	- poor performance for complex flows - robust, suitable for initial iterations - widely used
RNG $k - \epsilon$	- coefficients derived analytically - can model highly strained flows / swirling / low Re-number flows	- suitable for complex shear flows, vortex shedding behind bluff bodies
Realisable $k - \epsilon$	- adopts mathematical constraints for improved performance	- similar benefits / performance as RNG - possibly more accurate and easier to converge
Standard $k - \omega$	- two-equation model - superior performance for wall-bounded and low Re-number flows	- for complex boundary layer flows under adverse pressure gradients and separation - can be used for transitional flows - separation typically predicted to be excessive and early
$k - \omega$ SST	- uses standard $k - \epsilon$ model away from walls and standard $k - \omega$ near walls - optional compressibility	- similar performance to standard $k - \omega$ in most cases - no need for near wall modification
Reynolds Stress	- physically the most sound RANS model - suitable for complex 3D flows	- computationally demanding (in terms of CPU time, memory and convergence)

Table 3.1: Overview of the most commonly used RANS closure models

the overall dissipation rate

- σ_k and $\sigma\epsilon$: turbulent Prandtl numbers for k and ϵ

- S_k and S_ϵ: source terms

- $C_{1\epsilon}$, $C_{2\epsilon}$ and $C_{3\epsilon}$: constants, determined from experiments.

The turbulent viscosity depends on k, ϵ and density:

$$\mu_t = \rho C_\mu \frac{k^2}{\epsilon} \tag{3.19}$$

where C_μ is a constant.

3.4.2   k-ω

This empirical model is based on the turbulent kinetic energy (k) and specific rate of dissipation (ω), representing the dissipation rate of turbulence kinetic energy into internal thermal energy. The near-wall accuracy is higher than with the k-ϵ model, even with lower mesh resolution of the boundary layer [30]. However, the accuracy in the core of the flow-field remains inferior to the k-ϵ model. The transport equations are [1]:

$$\frac{\partial}{\partial t}\left(\rho k\right) + \frac{\partial}{\partial x_i}\left(\rho k u_i\right) = \frac{\partial}{\partial x_j}\left(\Gamma_k \frac{\partial k}{\partial x_j}\right) + G_k - Y_k + S_k + G_b \tag{3.20}$$

and

$$\frac{\partial}{\partial t}\left(\rho \omega\right) + \frac{\partial}{\partial x_i}\left(\rho \omega u_i\right) = \frac{\partial}{\partial x_j}\left(\Gamma_\omega \frac{\partial \omega}{\partial x_j}\right) + G_\omega - Y_\omega + S_\omega + G_{\omega b} \tag{3.21}$$

with the following quantities:

- G_k: generation of turbulence kinetic energy due to the mean velocity gradients,

- G_ω: generation of ω,

- Y_k and Y_ω: dissipation of and due to turbulence,

- Γ_k and $\Gamma\omega$: effective diffusivity of k and ω,

- S_k and S_ω: source terms, and

- G_b and $G_{\omega b}$: buoyancy terms.

The turbulent viscosity is computed according to Eq.3.22:

$$\mu_t = \alpha' \frac{\rho k}{\omega} \tag{3.22}$$

where α' denotes the optional dampening factor for low Reynolds number correlation.

3.4.3 $k - \omega$ Shear-Stress-Transport (SST) model

The Shear-Stress-Transport (SST) model combines the benefits of both, the $k - \epsilon$ and the $k - \omega$ model. The $k - \epsilon$ model is used far away from the wall boundary region and the $k - \omega$ model is employed close to wall boundaries [37]. Thereby, the weaknesses of $k - \epsilon$:

- over-prediction of the shear stress in adverse pressure gradient flows due to too low dissipation

- need for near-wall modification or modelling

are eliminated [12]. Similarly, the main disadvantage of $k - \omega$:

- dependence on the free stream value of ω

can be minimised. Due to its robustness and acceptable computational requirements [30], the $k - \omega$ SST model has become the industry standard and will be used for the simulations in this thesis.

3.5 Mesh requirements

One of the main challenges of a CFD simulation is to create a mesh that is fine enough to capture all of the relevant physics but at the same time computationally realisable and economical. For the present application, the mesh needs to be fine

at the separator walls to resolve the adherence of the fluid droplets and wall film buildup. Therefore, polyhedral cells with wall layer refinement were used. Fig.3.2 shows a horizontal cut of the meshed domain at the level of the separator inlet as well as the detail of the refined wall layer.

(a) Horizontal cross section of the meshed domain

(b) Wall layer refinement
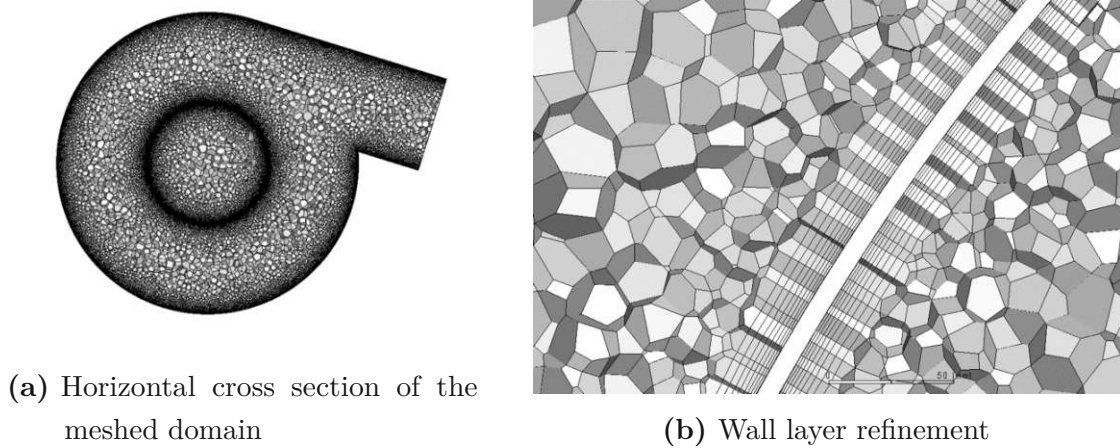
Figure 3.2: Mesh

3.5.1 y^+

y^+ is a non-dimensional distance of the wall-adjacent cell centre to the wall, expressing whether the flow in the wall-adjacent cells is in laminar or turbulent regime [47],

$$y^+ = \frac{u_\tau}{\nu} y \tag{3.23}$$

where ν describes the kinematic viscosity, y the distance from the wall and u_τ denotes the friction velocity:

$$u_\tau = \left(\frac{\tau}{\rho}\right)^{1/2} \tag{3.24}$$

where τ is the wall shear stress [8] and ρ is the fluid density. Within RANS simulations, there are two strategies of boundary layer treatment:

- resolving the whole boundary layer or

- using wall functions.

The decision, of which strategy is most suitable for the problem at hand, should be made on the basis of the importance of the boundary layer to the investigated

problem. If the boundary layer is not of primary interest, the usage of wall functions is strongly recommended, as they allow for mesh resolutions with y^+ values between 30 and 300. This reduces the number of volume cells required, and therefore, the computational time greatly. On the other hand, if the boundary layer is the main concern, it must be resolved in the simulations. In that case, $y^+ \approx 1$ is to be used.

3.6 Multiphase and droplet simulation

To simulate the droplet separator, a pure formulation for the gaseous flow is not sufficient. The fluid particle transport needs to be considered. Thus, the simulation approach must contain the models for the continuous phase (gas), the discrete phase (fluid), and for their interaction. Commonly, the continuous phase is modelled by the Eulerian formulation [49]. The discrete phase can be addressed either from Eulerian or from Lagrangian point of view. These combinations are name-giving for the respective formulations: Eulerian-Eulerian and Eulerian-Lagrangian [23]. Lagrangian perspective defines the particle characteristics along the particle path lines, whereas the Eulerian representation defines the trajectories in static volume cells. Both approaches are widely used and the choice for a particular flow field is largely dependant on the particle-fluid physics of interest [33].

3.6.1 Eulerian - Lagrangian formulation

In the Lagrangian reference frame, particles are treated discretely. The reference frame moves with the particles, i.e. the instantaneous location is determined from the reference of origin and the elapsed time. The flow properties need to be known since the tracking of individual particles relies on this information [26]. Using this strategy, ANSYS® FLUENT® provides the Discrete Phase Model (DPM) [38]. It solves the force balance equation for the discrete phase by tracking their trajectories through the calculated flow domain [43]. The model includes particle-particle interactions as well as interaction with the continuous phase. The DPM is restricted by the volume fraction of the dispersed phase and also allows only coalescence and collision of the same injected material [1]. An extensive elaboration on the Eulerian-Lagrangian methods can be found in [50].

3.6.2 Eulerian - Eulerian formulation

This approach models both phases as separate inter-penetrating and interacting fluids inside a single domain [4]. The governing equations are formulated accordingly and solved for each phase. The Eulerian approach computes both phases on a single grid, whereas the Lagrangian methods need interpolation of quantities between the fixed grids and the local position of particles [26]. The interactions need to be defined properly not only between the phases but also for each phase contacting the boundaries [51]. The particle velocities are calculated for each point of the domain. ANSYS® FLUENT® provides three Eulerian - Eulerian models: Volume of Fluid (VoF), Mixture and Eulerian model, where VoF is the most commonly used one. The model utilises the solution of the continuity equation to track the interface between the phases [1]:

$$\frac{1}{\rho_q}\left[\frac{\partial}{\partial t}\left(\alpha_q \rho_q\right) + \nabla \cdot \left(\alpha_q \rho_q \vec{u}_q\right) = S_{\alpha_q} + \sum_{p=1}^{n}\left(\dot{m}_{pq} - \dot{m}_{qp}\right)\right] \tag{3.25}$$

which responds to the phase q. $\dot{m}_{pq}$ describes the mass transfer from phase q to phase p and $\dot{m}_{qp}$ correspondingly from p to q. S_{α_q} is the source term, which is set to zero. α_q is the volume fraction of the phase q ranging from 0 to 1. The volume fraction itself is solved for the primary phase. The volume fraction is also defined for the density:

$$\rho = \sum\left(\alpha_q \rho_q\right) \tag{3.26}$$

and subsequently for the energy, which is defined as a mass-averaged value:

$$E = \frac{\sum_{q=1}^{n} \alpha_q \rho_q E_q}{\sum_{q=1}^{n} \alpha_q \rho_q} \ . \tag{3.27}$$

Chapter 4

Problem definition

This chapter provides the background to the investigated problem as well as the operating conditions. Additionally, the geometrical adaptations are discussed.

4.1   Geometry

The main concerns with regard to computational strategy are scale differences, i.e. the extensions of the separator and the water droplet size. The need for a fine mesh is opposed by the geometrical dimensions, as the size of industrially installed droplet separators reaches a few meters in height and diameter. The required mesh cannot be created on a standard computer, as approximately 200GB of memory are needed. The meshing as well as the computations have been carried out on the Vienna Scientific Cluster (VSC), which is described in more detail in Section 5.1.

4.2   Boundary conditions

The computations are performed with boundary conditions provided by the site operator. The inlet mass flow rate, the outlet pressure, and the operating temperature are known. These are set in ANSYS® FLUENT®, as described in Chapter 5.2.3.

4.3 Variant a - reference state

The droplet separator in its current state does not reach the expected separation efficiency, which threatens damage to the downstream equipment, i.e. the compressor. The need for cleaning and therefore for production interruptions has severe implications for the site operator. This variant of the droplet separation is named Variant a in the evaluation section.

4.4 Suggested adaptations

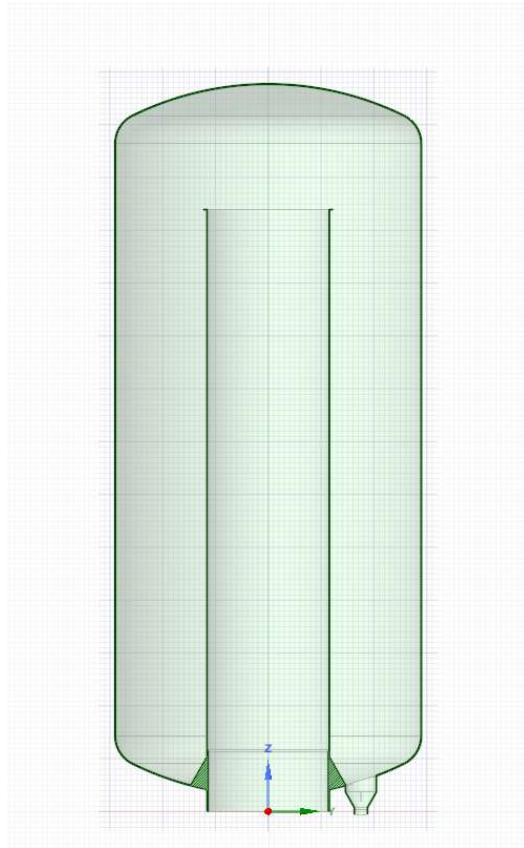### 4.4.1 Variant b - enlargement of the droplet separator

The height of the separator is increased by 25%, see Fig.4.1a, which provides the water droplets more time to separate on the walls. There are several factors contributing to this choice:

1. Existing design: The separator had been designed in form of equally high modules, corresponding to 25% of its total height. E.g. the distance between the two inlets, as well as lower outlet to lower inlet is the equal.

2. Material availability: Common and therefore cost-effective size.

3. Statics: The weight of the separator should not be altered significantly such that a new support structure is needed.

4. Computational effort: The height enlargement means more volume that must be discretised. The computations are all memory-bound. Therefore, any need for more memory must be well justified.

4.4.2 Variant c - upside-down installation

For this variant, the droplet separator is turned upside down, see Fig.4.1b. The placement of the fluid outlet had to be adapted to the lowest part in the centre. Otherwise the geometry remains unchanged. The mode of operation would change to a classical cyclone. The main idea of this design is the possibility of integrating active cleaning of the walls during operation. Active cleaning could be considered

in the future, the simulation of the upside-down installation is performed without additional cleaning.

(a) Mid-plane cut of the separator enlarged by 25%.
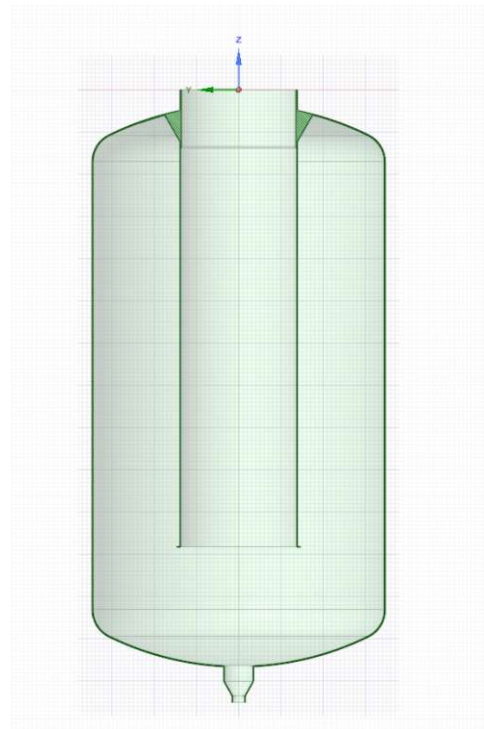
(b) Mid-plane cut of the droplet separator turned upside down.

Figure 4.1: Adaptations: Variant b and Variant c

Chapter 5

Solver setup

The aim of this chapter is to identify the most suitable simulation setup in ANSYS®
FLUENT®.

5.1 Computational resources

The simulation as well as pre- and post-processing were conducted on the VSC-4
of the Vienna Computational Cluster. An interactive node with the following
characteristics was used for meshing, case definition, and post-processing:

- CPU: AMD EPYC 7302P, 3GHz,

- RAM: 256GB, and

- 32 cores.

Due to mesh size, more memory was required for the computation. Thus, a
computational node of the VSC-4 was used, which had the following characteristics:

- CPU: Intel Xeon Platinum 8174, 3.1 - 3.9GHz,

- RAM: 768GB or 384GB, and

- 48 cores.

5.2 Implementation in ANSYS® FLUENT®

5.2.1 General settings

The basic settings were chosen as follows:

- Solver type: Pressure based

- Time: Steady state

- Space: 3D

- Gravity: on

The choice of the pressure-based solver results from further need for models which are enabled only with pressure based solver. Due to the size of the droplet separator and also due to the constant mass flow and temperature, the steady state simulation has been chosen. The outflow of the fluid relies on gravity, therefore the usual gravitational acceleration of 9.81 m/s^2 in negative z-direction is used. In regards to geometry, the droplet separator itself as well as the flow are non-symmetric in all direction and therefore need a full 3D simulation.

5.2.2 Turbulence, Multiphase and other model settings

Turbulence

Due to reasons described in Chapter 3.3, the SST $k - \omega$ turbulence closure model was selected.

Multiphase model

The multiphase nature of the flow needs to be considered due to the interaction phenomena between water and steam. There are two interaction modes: water droplets can form by collision and interaction with the steam, and water films can form by adhesion at the separator walls.

The multiphase model was an unexpected challenge while setting up the simulations. Although suggested by literature [1, 42] as the most suitable multiphase model for

cyclones, the mixture model turned out to be unsuitable for the problem at hand. The low steam density compared to the water density resulted in high velocity gradients, which caused solution divergence in the continuity equation. The problem could be partially solved using the VoF model, which allows for a dispersed phase interface. The wet-steam model was also considered, but could not be applied due to the limitation of liquid phase mass fraction to 0.2. Water accumulates at the lower drainage, which rules out any successful computation with the wet steam model. As a workaround, splitting the domain was considered. This modelling strategy turned out to be inapplicable, as ANSYS® FLUENT® does not allow the multiphase model being applied only to a part of a domain. The Eulerian model was not considered due to its computational cost. The application of the VoF model was only possible up to a certain vapour mass flow rate (approximately 70% of the target mass flow rate). [1] Considerable time and computational resources were used to find a proper setup, without success. The model behaviour would require further investigation. The final choice was to employ a single-phase approach, where the water droplets were one-way coupled to the vapour flow field. The domain was adjusted, such that the lower drainage with the standing water was substituted by a boundary with the physical properties of a water surface. The adjusted domain of the basic geometry is shown in Fig. 5.2. This allowed for a finer mesh and revised solution strategy. The vapour flow is simulated as a single-phase flow. The water

---

[1]Beyond 70% of the target mass flow rate, the VoF model caused in unphysical flow phenomena, leading to extreme values of turbulent viscosity ratio, temperature and pressure, which caused numerical divergence. Some of these encountered phenomena are plotted in Fig. 5.1.

(a) Disturbed water surface

(b) Water pushed out of the separator

(c) Formation of a water jet
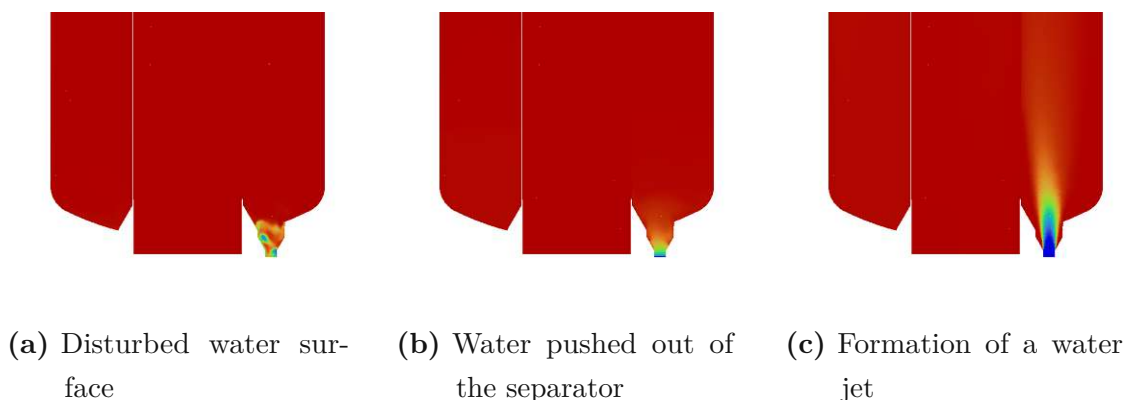
Figure 5.1: Wrong behaviour of the VoF model. The plot shows the volume fraction of vapour from 0 (blue) to 1 (red) of the mid-plane cross-section.
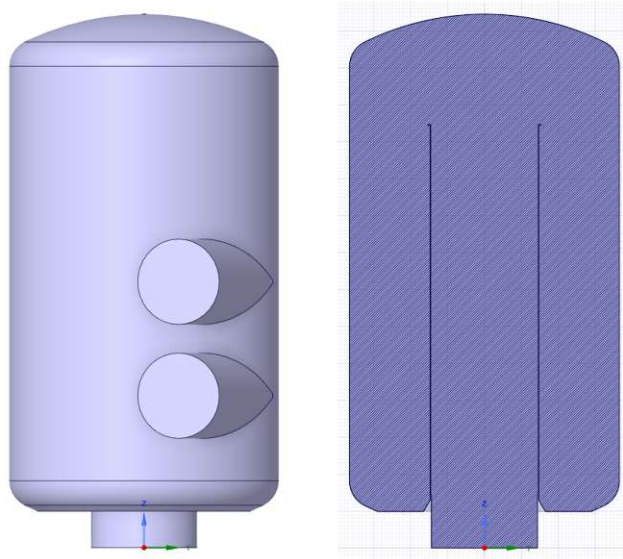
Figure 5.2: Simplified domain

droplets were considered by a coupling of the Discrete Particle Model (5.2.2) and Eulerian Wall Film Model (5.2.2), as suggested by [2, 41].

Discrete particle model

In order to model the particles, the DPM model is utilised. The theory can be found in Chapter 3.6.1. The size, total mass flow and distribution of particles, as well as their material are regulated via DPM Injections. In this case, the injections were set to be uniform in distribution over the inlet surfaces. Particle size and total droplet mass flow were varied, to test the separator efficiency. The test cases can be found in Tab. 5.1.

Eularian wall film model

The Eulerian Wall Film Model (EWFM) is used to enable water condensation on the walls as well as to model the resulting water film [55]. By setting the film material to the same as the water droplet of the DPM model and allowing the DPM - EWFM coupling the droplet separation is allowed [24].

5.2.3   Boundaries

Inlet

The vapour mass flow rate is specified at the inlets. Simultaneously, the inlet surfaces serve as the injection surfaces for the water droplets.

Walls

The walls are specified as no-slip boundary conditions with the ability to build up an Eulerian wall film by trapping the water particles in the DPM model.

Water surface

The liquid water level is substituted by a boundary with the physical properties of a water surface. The water surface is able to trap the water particles of the DPM model.

Outlet

The vapour outlet is realised as a pressure outlet with prescribed static pressure with radial pressure equilibrium distribution (due to the swirling motion of the vapour). The water droplets can escape through this boundary.

5.2.4   Numerical schemes

The pressure-based solver was selected using the SIMPLEC scheme for pressure-velocity coupling. The cell-based least-squares scheme was used for gradient discretisation and second-order upwind schemes were employed for the convective terms of flow momentum, turbulent kinetic energy, specific dissipation rate, and energy. Consistently, second-order discretisation was used for continuity, flow momentum, and energy equations in the Eulerian wall film model.

5.2.5   Tested configurations

27 simulation cases have been considered resulting due to the combination of the three geometries, three droplet mass flows, and three droplet size distributions. The investigated geometry variants are shown in Fig. 5.3. The mass flow rate and the droplet diameter combinations can be found in Tab. 5.1.
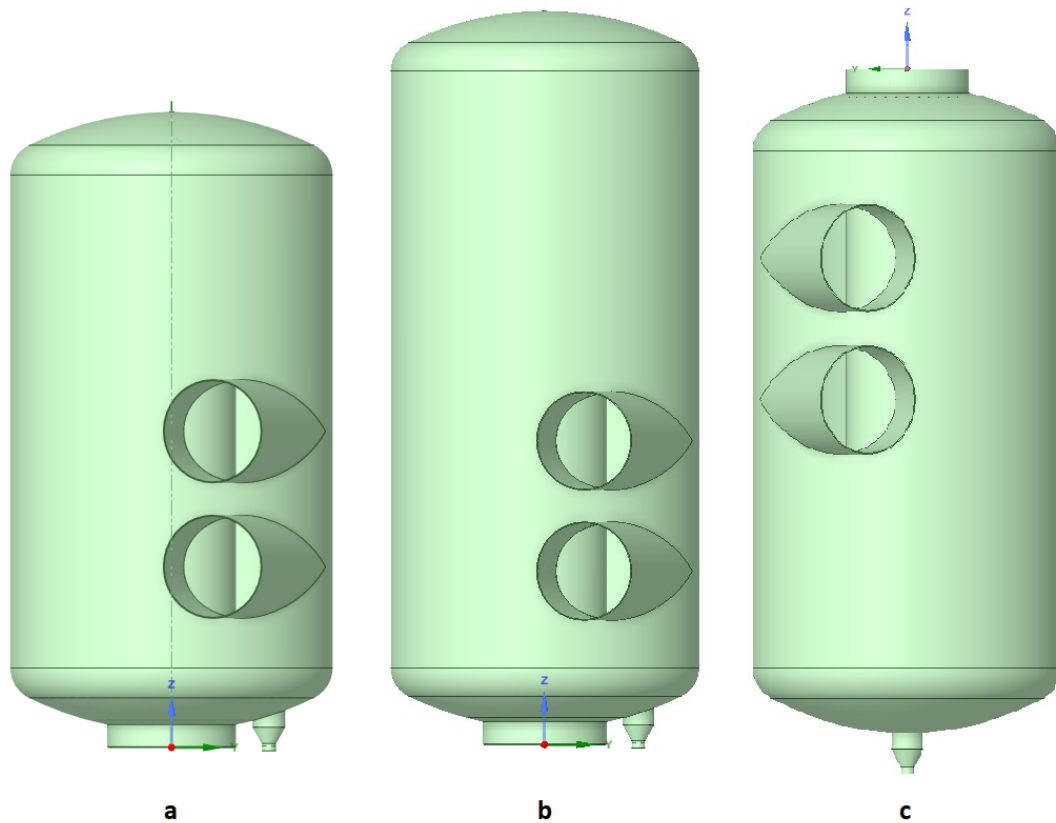
Figure 5.3: Investigated geometry variants. a: current state, b: enlarged separator, c: upside-down installation

Case	Droplet mass flow in kg/s	Droplet diameter in mm
1	0.1	0.001 - 0.01
2	0.1	0.01 - 0.1
3	0.1	0.1 - 0.2
4	1.0	0.001 - 0.01
5	1.0	0.01 - 0.1
6	1.0	0.1 - 0.2
7	10	0.001 - 0.01
8	10	0.01 - 0.1
9	10	0.1 - 0.2

Table 5.1: Tested water droplet cases

Chapter 6

Simulation results

The results of the numerical simulation are presented in this chapter. All configurations were computed for 7000 iteration steps. The flow results are presented as comparison of the three geometries, whereas the droplet separation results contain all of the evaluated cases described in Section 5.2.5.

6.1   Velocity

The velocity evaluation is presented in the form of velocity contour plots in the mid-plane cross-section as well as velocity profiles. The profile locations were chosen such that the effects of the inlets and the pipe vortex region are minimal. All velocity values were normalised by the inflow velocity.

Figure 6.1 compares the velocity magnitude contours. The maximal velocities occur at the inlet of the inner cylinder. Variants a and c reach a maximum of 4.55 and 4.56 times the inflow velocity. Variant b exhibits 5.5% lower maximal velocities. Additionally, Variants a and c show a slight asymmetry shortly after the entrance into the inner cylinder. The horizontal in-plane component of the velocity is shown in Fig. 6.2. As expected, this component remains negligible in most parts of the domain. The only exception occurs at the inlet into the inner cylinder, where the flow is radially accelerated. The normal-to-plane velocity is shown in Fig. 6.3. While Variants a and c show nearly identical maxima, Variant b reaches approximately 8% lower maximal velocities. The vertical velocity contours are shown in Fig. 6.4, revealing again that the flow field is generally equivalent.

The maxima of the vertical velocity component which occur at the inlet of the inner cylinder, are slightly different between all configurations.
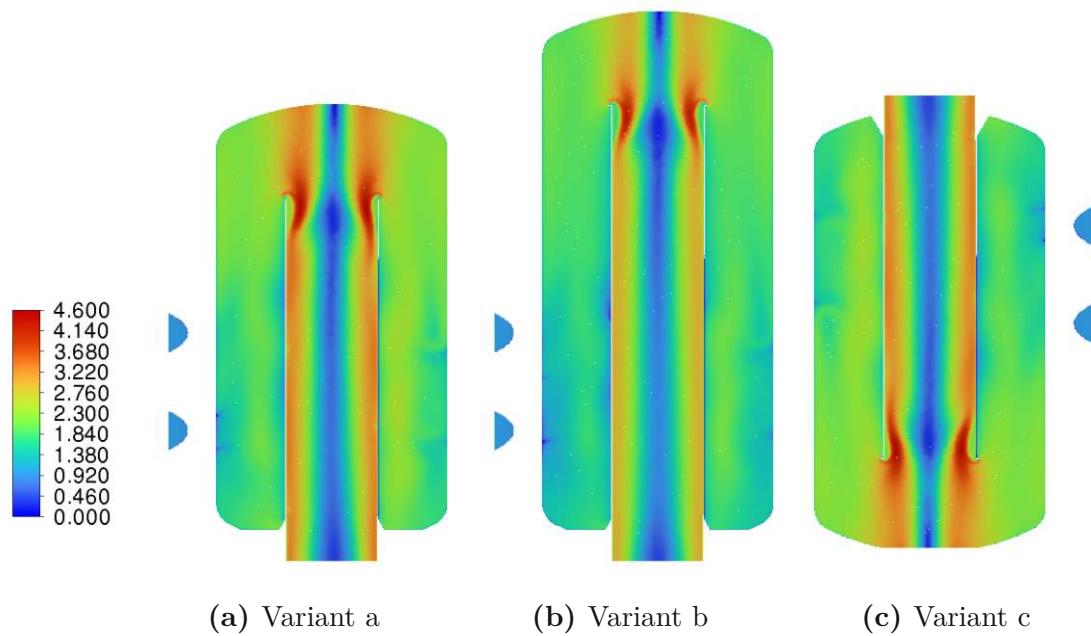

(a) Variant a   **(b)** Variant b   **(c)** Variant c

Figure 6.1: Velocity magnitude normalised by inflow velocity

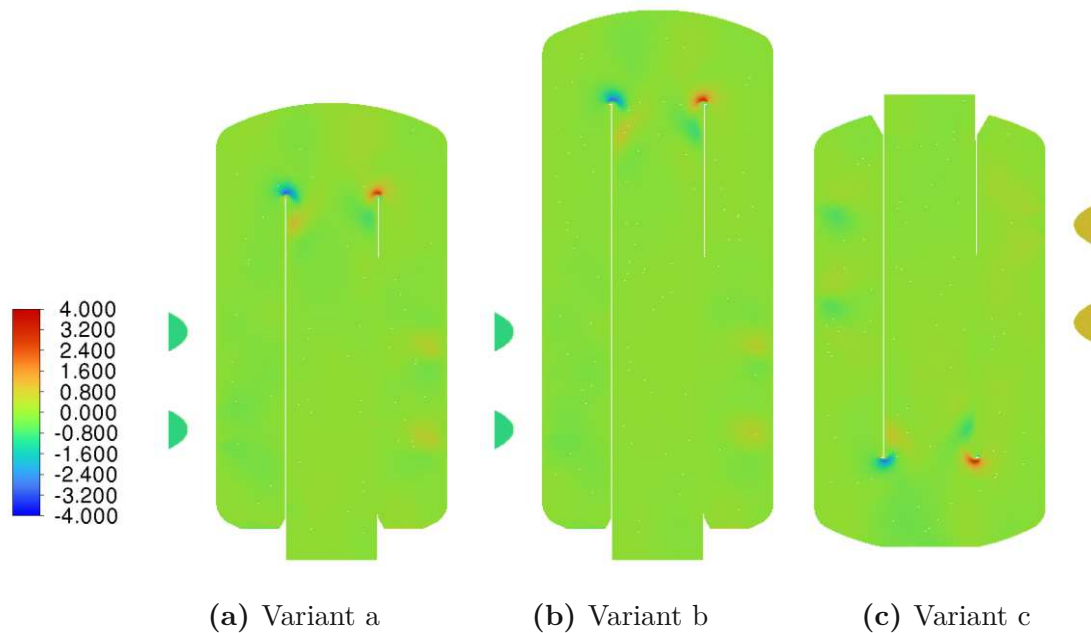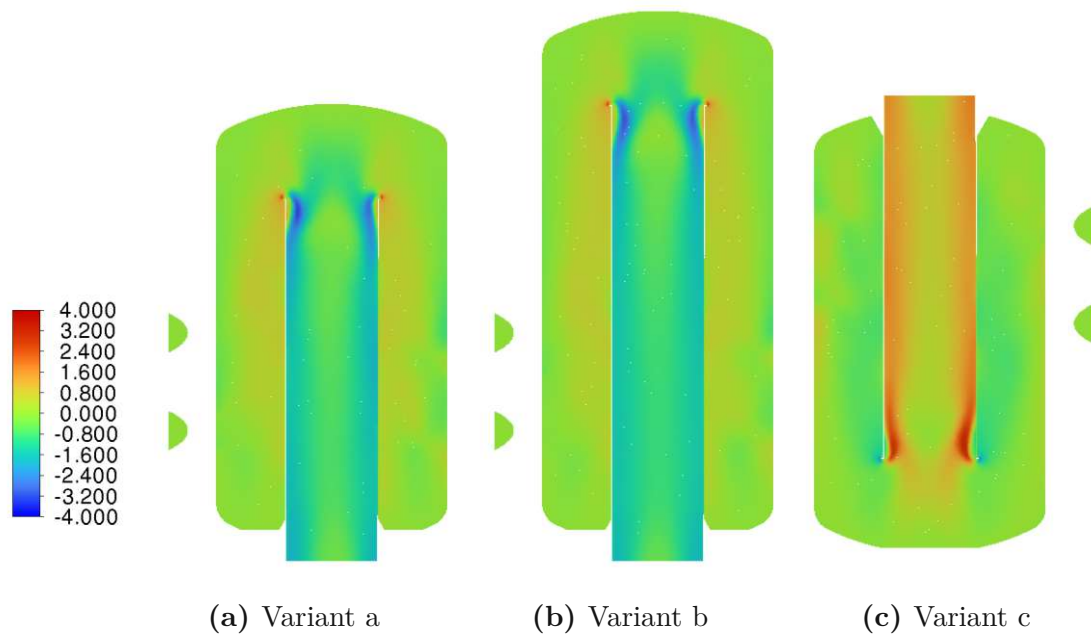**(a)** Variant a   **(b)** Variant b   **(c)** Variant c

Figure 6.2: In-plane horizontal velocity component normalised by inflow velocity

(a) Variant a   **(b)** Variant b   **(c)** Variant c
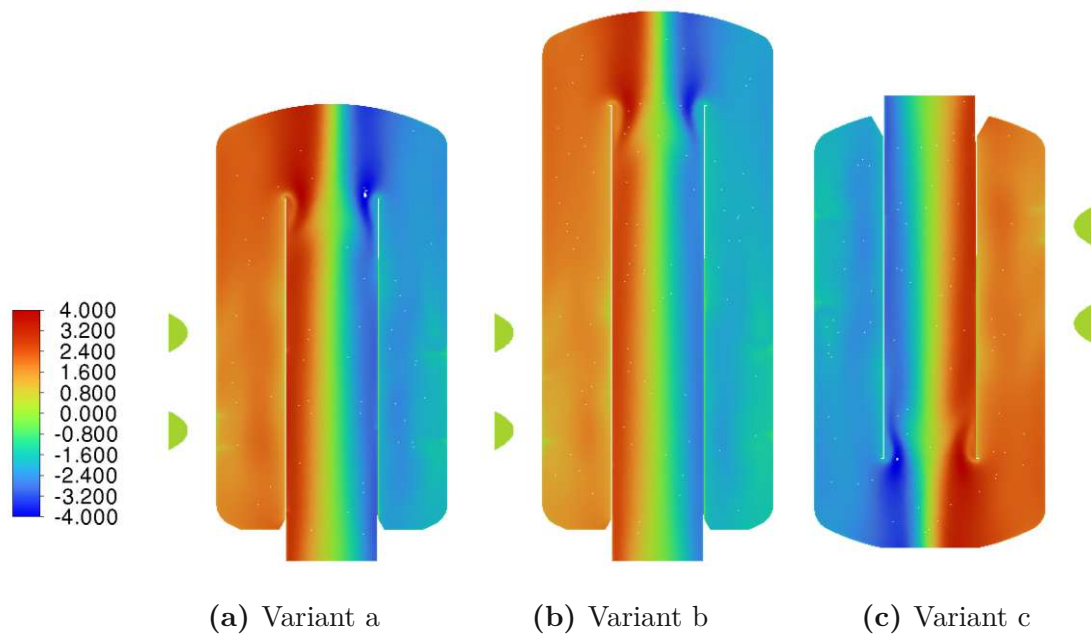
Figure 6.3: Normal to plane horizontal velocity component normalised by inflow velocity

(a) Variant a   **(b)** Variant b   **(c)** Variant c

Figure 6.4: Vertical velocity component normalised by inflow velocity

As for the velocity profiles, shown in Fig. 6.5, one can see that the in-plane horizontal velocity components remain insignificant in all cases. The vertical velocities resemble the "W" (Variant a and b) or "M" shape (Variant c) typical for a strongly rotating flow. In the outer annular pipe, the vertical velocity is positive regarding the main flow direction in the inner part and negative in the outer part. The presence of such an inflection point indicates instability and therefore an unsteady flow. As stated above, the velocity profile of Variants a and c is not completely symmetric, showcased by the maximum of the normal-to-plane velocities.
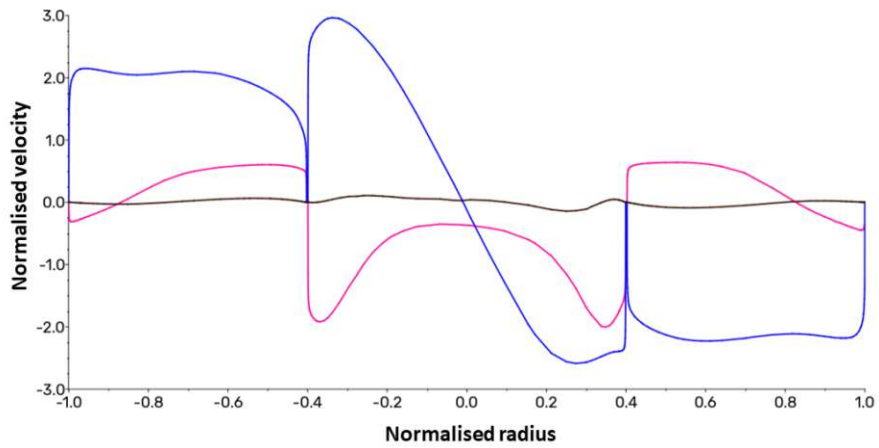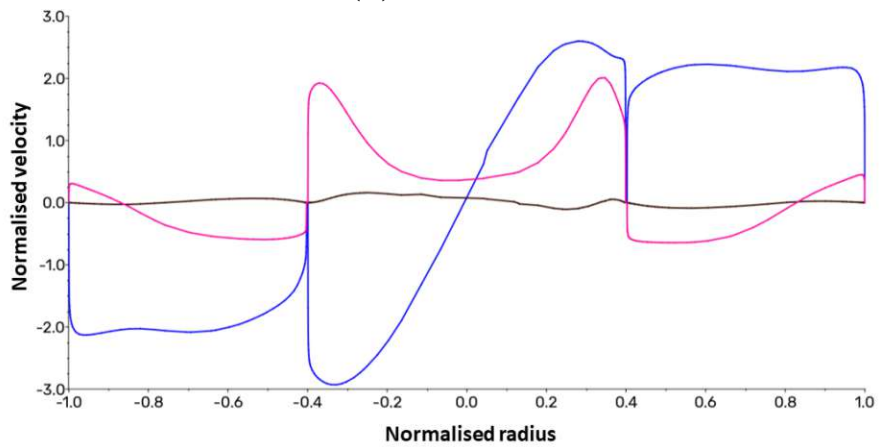
(a) Variant a
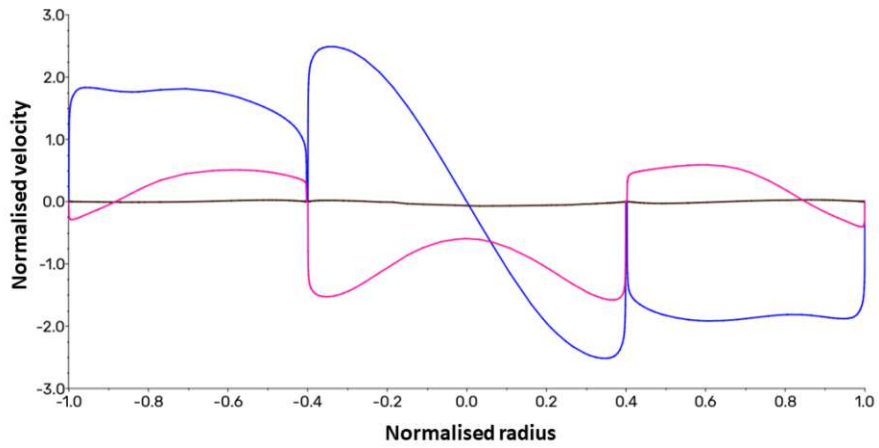
**(b)** Variant b

(c) Variant c

Figure 6.5: The flow velocities normalised by inflow velocity. Vertical velocity is plotted in magenta, radial velocity is plotted in blue and in-plane velocity is plotted in brown

6.2 Turbulence

Turbulent kinetic energy is commonly used to visualise the locations of flow fluctuations, as it is defined as the root mean square of the fluctuation components of the flow velocity. In fluid dynamics, it can simply be defined as the mean kinetic energy per unit mass for a turbulent flow. The turbulent kinetic energy contours are shown in Fig. 6.6 for all Variants. The region of the inner cylinder entrance experiences the maximal values which correlates with the maximal velocity gradients. The shape of the most turbulent region is the same for all Variants. The absolute maxima are equal for Variants a and c, whereas the maximal turbulent kinetic energy is approximately 11% lower for Variant b. The y^+ evaluation reveals the following values:

- Variant a:

  - max.: 17.96

  - area - averaged: 15.15

- Variant b:

  - max.: 27.29

  - area - averaged: 13.2

- Variant c:

  - max.: 29.49

  - area - averaged: 14.61

The ideal y^+ value should be below 1. However, a mesh with such refinements would require a multiple of the available computational resources.

(a) Variant a   **(b)** Variant b   **(c)** Variant c
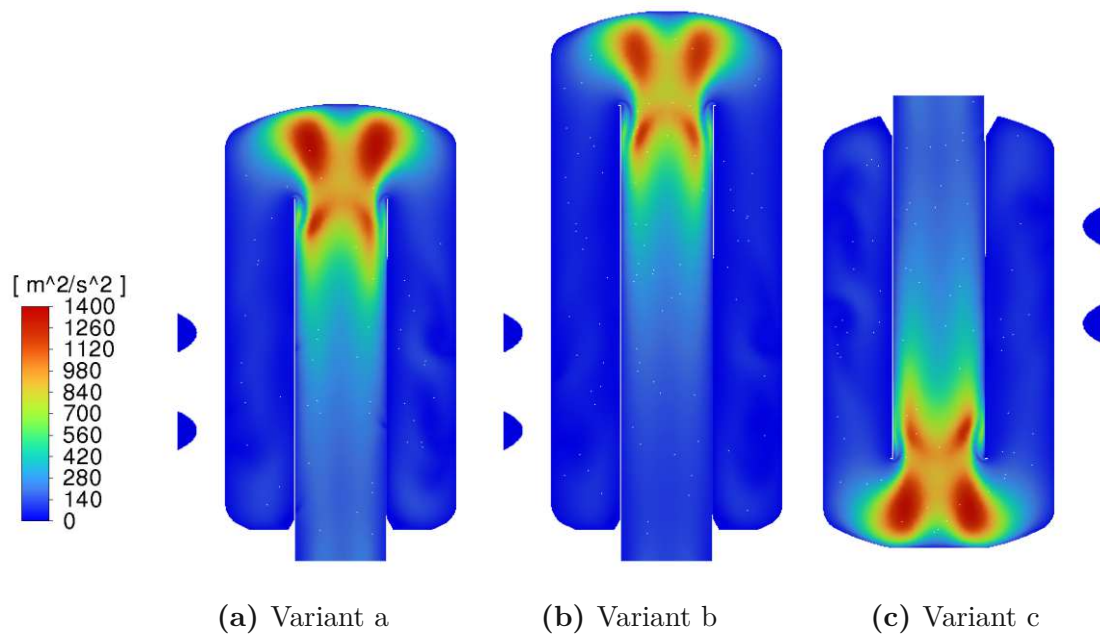
Figure 6.6: The turbulent kinetic energy $[m^2/s^2]$ contours are show in the mid-plane view.

6.3 Pressure

The static pressure evaluation can be seen in Fig 6.7. The values are normalised by the outlet static pressure. Noteworthy is that the outlet static pressure is calculated as an area-averaged value due to the non-uniform distribution over the outlet surface caused by the swirling flow.

The values are higher in the outer circumference of each cylinder and lower in the centre. This is the expected result of the centrifugal forces implied by the swirling flow. The pressure variation in Variant b are lower than in the other two variants. More concretely, the values range from 0.95 to 1.09 for Variant b and from 0.94 to 1.11 for the remaining Variants. The reason for this observation is the lower velocity, and therefore, lower swirl and centrifugal forces.

The pressure drop was also evaluated, presented in the form of a percentage of the outlet static pressure:

- Variant a: 11.15%

- Variant b: 9.35%

- Variant c: 11.06%

Surprisingly, the pressure drop of the enlarged geometry is the lowest. Further investigations would be needed to understand this phenomenon.

(a) Variant a   **(b)** Variant b   **(c)** Variant c
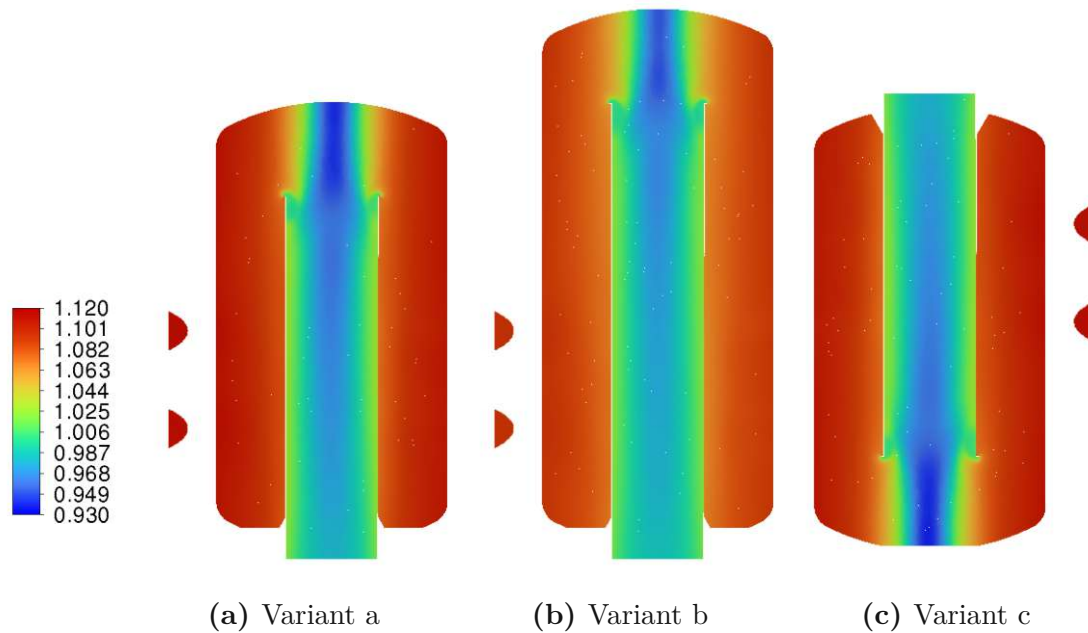
Figure 6.7: Static pressure normalised by outlet static pressure.

6.4 Droplet separation

The droplet separation evaluation is presented in Tab. 6.1, 6.2 and 6.3 for the three geometry variants. The total amount of droplets was 22562 for Variant a, 22840 for Variant b and 22552 for Variant c. The meaning of the abbreviations in the tables is as follows:

- Escaped: amount of particles which were not separated

- Trapped: amount of particles which impinge the water surface

- Incomp.: incomplete; trajectories of these particles which did not end at any boundary

- EWF abs.: Eulerian wall film absorbed; amount of particles interacting with solid surfaces and being absorbed by the Eulerian wall film

- % NOT sep.: percentage of particles falling into categories escaped or incomplete with respect to the total amount of tracked particles.

Case	Escaped	Trapped	Incomp.	EWF abs.	% NOT sep.
1a	2801	280	4	19477	12.43
2a	2822	276	4	19460	12.53
3a	2820	271	4	19467	12.52
4a	5	41	0	22516	0.02
5a	5	40	0	22517	0.02
6a	6	39	0	22517	0.03
7a	0	0	0	22562	0.00
8a	0	0	0	22562	0.00
9a	0	0	0	22562	0.00

Table 6.1: Droplet separation results; Variant a

The results show that the separation effectivity is strongly dependent on the droplet size. The largest droplets (0.1 - 0.2 mm in diameter) impinge on the separator walls directly upon entering regardless of the geometry variant. Their trajectories are not affected by the flow direction. All three separator variants are capable of separating all droplets in this diameter range.

In the intermediate diameter range (0.01 - 0.1 mm), slight differences in separation ability emerge. Although all variants are to be described as functioning effectively, Variant b and Variant c are capable of separating 99.99% of the droplets, Variant a reaches a success rate of 99.97 - 99.98%. The highest differences are observed when considering the smallest evaluated droplet diameters (0.001 - 0.01 mm), computed as the mean value of the considered droplet mass flow rates:

- Variant a: 12.49% not separated

- Variant b: 11.69% not separated

- Variant c: 12.55% not separated

Clearly, the separator type reaches its limits and is not suited for the smallest droplets. Variant b is more effective, providing more rotations and therefore time for the droplets to impinge. The total droplet mass flow rate does not influence the

separation efficiency as long as an adequate water outflow is provided. Therefore, the droplet trajectories remain the same and are shown exemplarily in Fig. 6.8 for the total droplet mass flow rate of $0.1 kg/s$. As visible from the colour-code, the smaller the droplets, the longer they remain in the flow. Non-separated droplets of the intermediate diameter category come exclusively from the lower end of the diameter range. In the case of the smallest droplets, this trend is no longer present to such an extent.

Case	Escaped	Trapped	Incomp.	EWF abs.	% NOT sep.
1b	2652	241	2	19942	11.62
2b	2678	230	4	19928	11.74
3b	2673	235	4	19928	11.72
4b	2	31	0	22807	0.01
5b	2	27	0	22811	0.01
6b	3	30	0	22807	0.01
7b	0	0	0	22840	0.00
8b	0	0	0	22840	0.00
9b	0	0	0	22840	0.00

Table 6.2: Droplet separation results; Variant b

Case	Escaped	Trapped	Incomp.	EWF abs.	% NOT sep.
1c	2838	191	9	19514	12.62
2c	2813	173	5	19561	12.50
3c	2820	271	4	19467	12.52
4c	2	10	0	22540	0.01
5c	3	10	0	22539	0.01
6c	2	9	0	22541	0.01
7c	0	0	0	22552	0.00
8c	0	0	0	22552	0.00
9c	0	0	0	22552	0.00

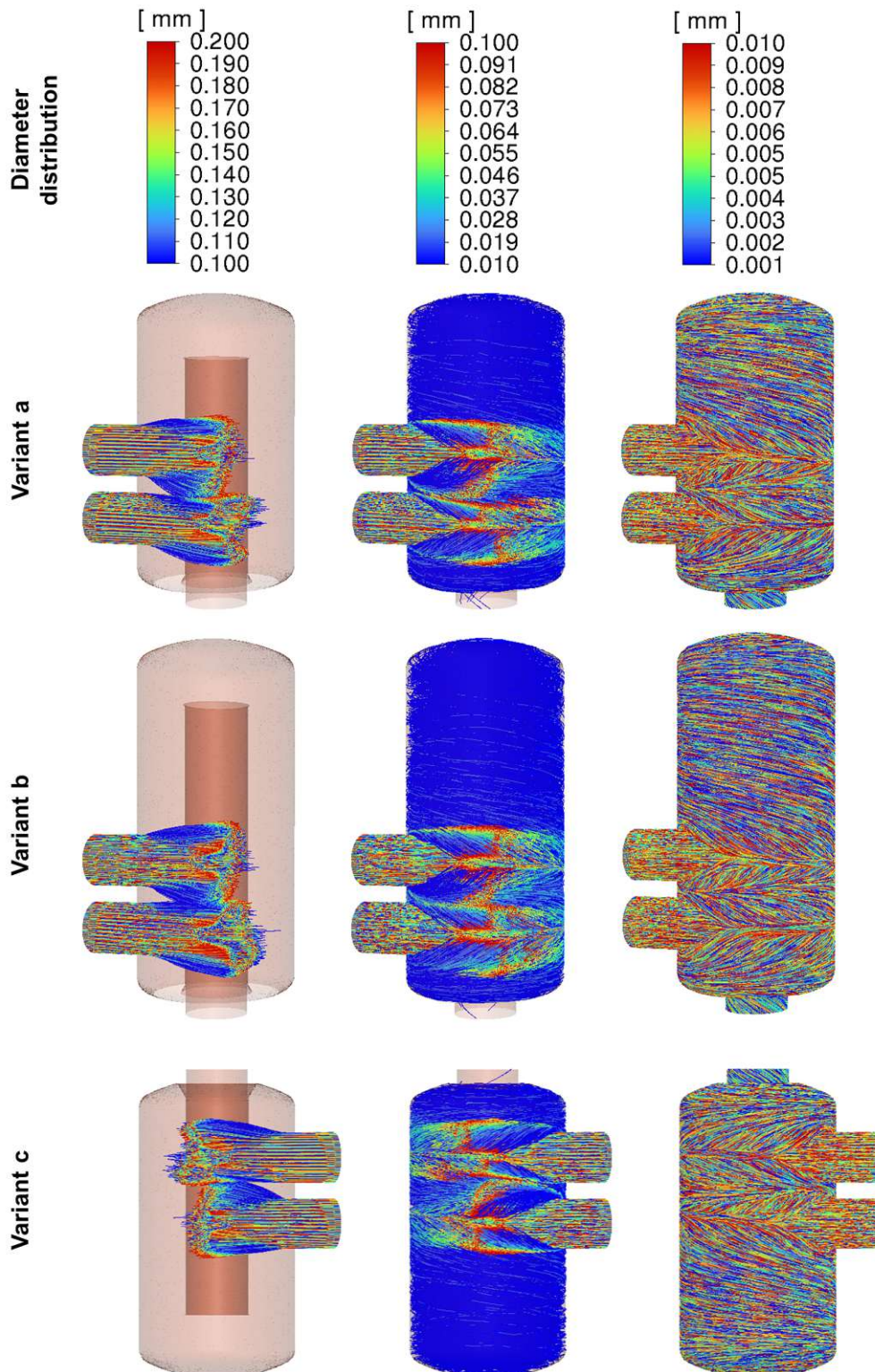**Table 6.3:** Droplet separation results; Variant c

Figure 6.8: Droplet path lines shown for a total droplet mass flow rate of $\dot{m} = 0.1$ kg/s.

6.5   Excursus: Reduced vapour mass flow

Variant a is analysed at a second operating condition with a reduced vapour mass flow rate to 1/3, which also reduces the inlet velocity to 1/3. All velocities and pressures are normalised by the inflow velocity and the resulting outlet static pressure, respectively. As visible in Fig. 6.9a, the inflow velocity is low, and therefore, secondary swirls form in the outer cylinder. Figure 6.9b shows the regions of positive vertical velocities and indicates that negative vertical velocities occur in a large part of the domain. Interestingly, a backflow emerges at the centre of the vapour outlet.

**(a)** Normalised velocity magnitude   **(b)** Positive vertical velocity regions
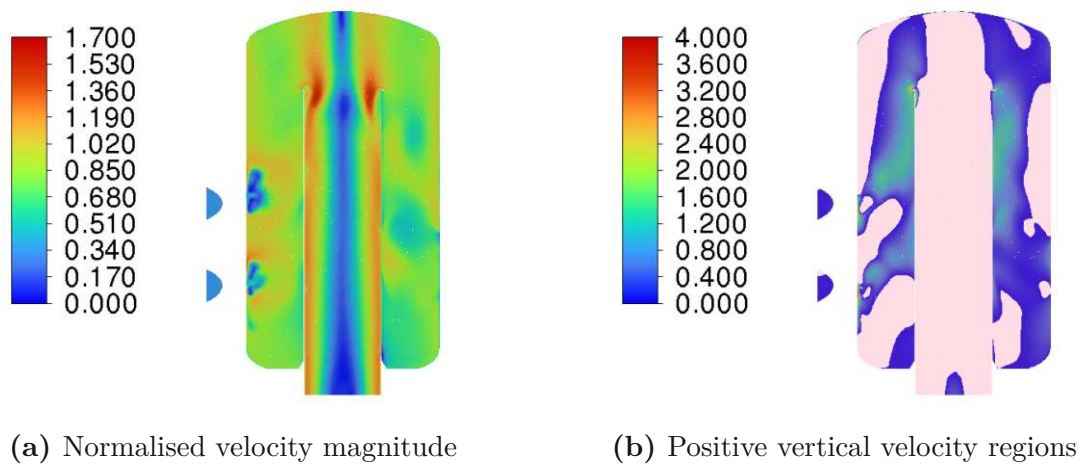
Figure 6.9: Normalized velocity for the reduced inlet velocity

The velocity profiles (Fig. 6.10), evaluated at the same location as for Variant a, resemble the velocity profiles of Variant a only for the vertical velocity. The in-plane horizontal velocity shows a significant non-symmetry.

The static pressure contours are depicted in Fig. 6.11a. The pressure distribution is perturbed by the large-scale flow structures in the outer cylinder, particularly the inlet zone. The pressure drop remains low, with only 1.38% of the area-averaged outlet static pressure. As expected, due to the lower velocities, the turbulent kinetic energy values, shown in Fig. 6.11b remain almost an order of magnitude lower than for the prior investigated operating condition. The highest values are still reached at the inlet into the inner cylinder. Relatively high turbulent kinetic energy levels are also present in the outer cylinder. The y^+ values correspond to the lower
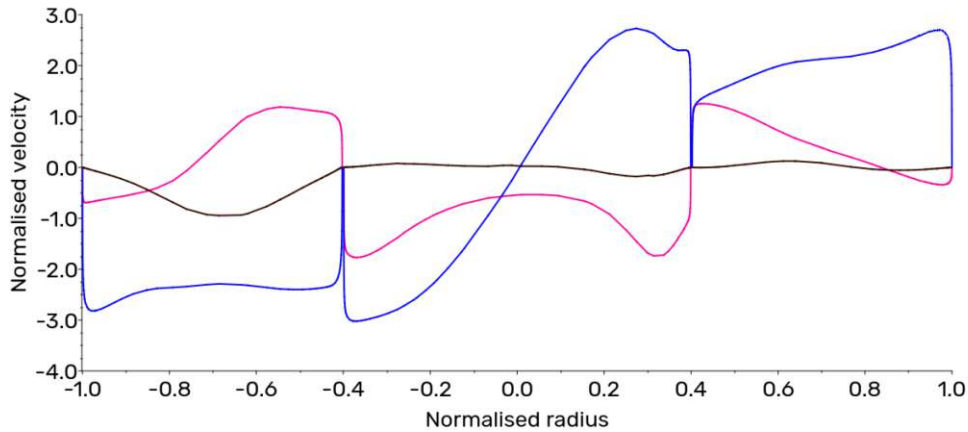
Figure 6.10: The flow velocities are normalised by reduced inflow velocity. Vertical velocity is plotted in magenta, radial velocity is plotted in blue and in-plane velocity is plotted in brown

velocity, with a maximum of 18.14 and an area-averaged value of 6.94.

(a) Normalised static pressure

(b) Turbulent kinetic energy
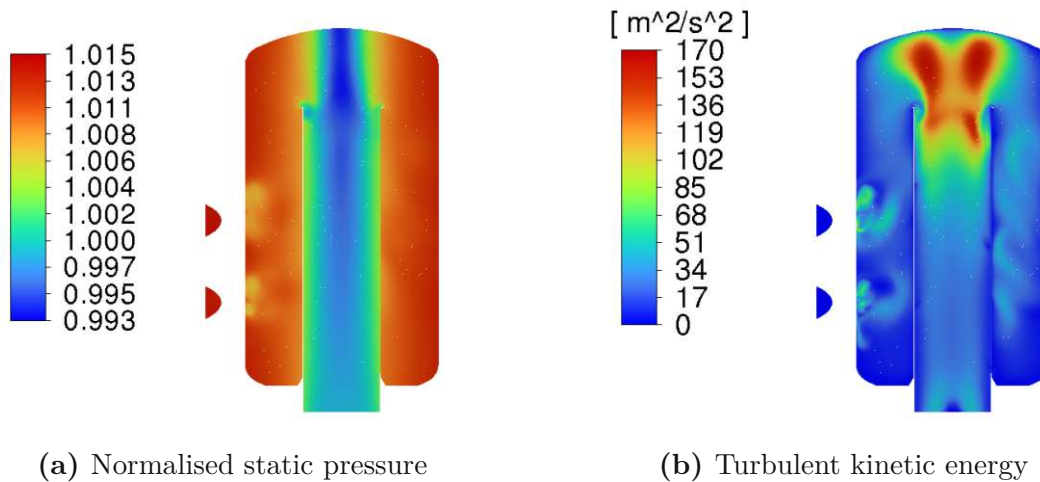
**Figure 6.11:** Pressure and turbulence evaluation

The droplet separation capacity was evaluated using the same droplet diameter distributions as before, the total droplet mass flow was restricted to the case of $0.1 kg/s$. The results in Tab. 6.4 show that the largest droplets are separated equally well as for the other operating conditions. However, 0.76% of the water particles with intermediate diameter distribution were not separated. Similarly, the largest water droplets are separated poorly, with 20.48% not separated, compared

to 11.62 - 12.62% for the other operating conditions. The path lines are shown in Fig. 6.12.

Case	Escaped	Trapped	Incomp.	EWF abs.	% NOT sep.
0.001 - 0.01	4502	91	118	17851	20.48
0.01 - 0.1	170	7	1	22384	0.76
0.1 -0.2	0	0	0	22562	0.00

Table 6.4: Droplet separation results; Reduced vapour mass flow; total droplet mass flow $\dot{m} = 0.1 kg/s$

The results show that this separator geometry is not functional at operating conditions with lower velocities. The flow field reveals large recirculation regions and the droplet separation effectivity is considerably worsened.

(a) 0.001 - 0.01 mm   **(b)** 0.01 - 0.1 mm   **(c)** 0.1 - 0.2 mm
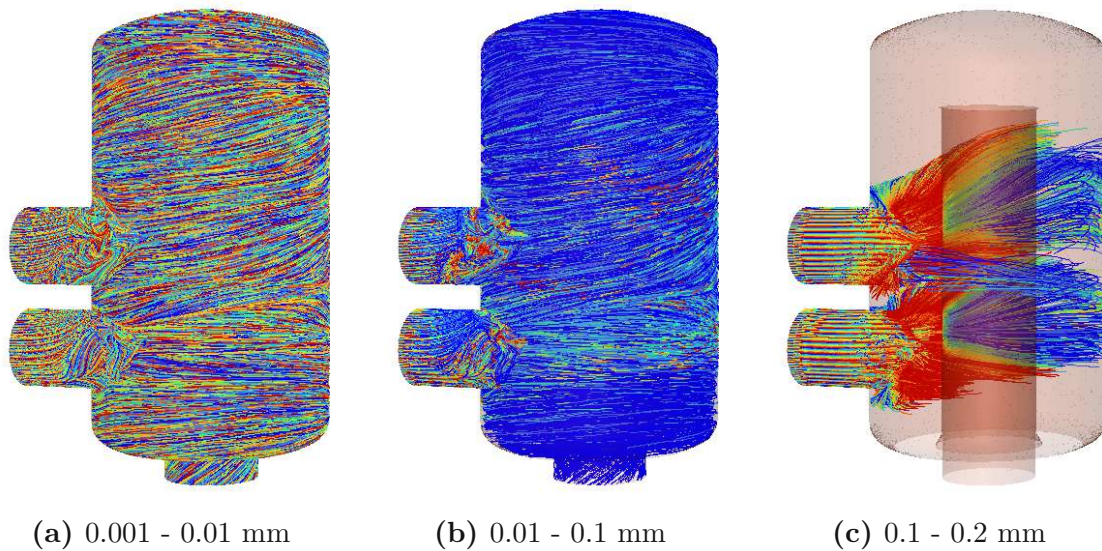
Figure 6.12: Droplet path lines shown for a total mass flow rate of $\dot{m} = 0.1\ kg$.

Chapter 7

Conclusions

Three different droplet separators have been evaluated in terms of flow and droplet separation characteristics. Variant a (basic geometry) and Variant c (upside-down installation) have been found to operate similarly. Their respective velocity and pressure profiles do not reveal significant differences. The calculated maxima of velocity as well as pressure compare well. The droplet separation is also similarly successful for the largest and smallest droplets. For the intermediate-sized droplet diameters, Variant c reaches higher efficiencies, comparable to Variant b (enlarged separator height). Variant b is superior in separating the smallest scale droplet particles compared to both other variants. Variant b exhibits also the most differences in flow topology. The velocity maxima and the maximal turbulent kinetic energy are the lowest. Surprisingly, the pressure drop of this variant is also the lowest. The numerical simulation results show that Variant b is the most efficient droplet separator.

The following results are valid for all variants. The total droplet mass flow does not influence the separator efficiency. This result has to be understood in the limits of the simulation assumptions, more concretely as a result of steady state, one-way coupled simulation with secured water drainage. None of the evaluated variants is capable of the complete separation of the smallest droplets. Another separator type would be needed in addition. The results also indicate unsteady flow phenomena. Therefore, a validation of the computed results in the form of measurements is recommended. Subsequently, a transient simulation and mesh refinement is advisable.

The main outcome of the numerical simulation of the three different droplet separators can be summarised by the following points:

- The effectivity of the separator is highly dependent on the droplet size.

- There are considerable differences among the tested variants, mainly due to separator dimensions, with Variant b being the most effective.

- The functionality is independent of the total droplet mass flow.

- To achieve complete separation of the smallest droplets, a combination with another separator type is necessary.

Bibliography

[1]   Ansys Inc. Ansys Fluent Theory Guide, 2021.

[2]   Anzai, H., Shindo, Y., Kohata, Y., Hasegawa, M., Takana, H., Matsunaga, T., Akaike, T., and Ohta, M. (2022). Coupled discrete phase model and Eulerian wall film model for numerical simulation of respiratory droplet generation during coughing. *Scientific reports 12*, 14849.

[3]   Bailey, A. G., Balachandran, W., and Williams, T. J. (1983). The rosin—rammler size distribution for liquid droplet ensembles. *Journal of Aerosol Science 14*, 39–46.

[4]   Balakin, B. V., Hoffmann, A. C., Kosinski, P., and Rhyne, L. D. (2014). Eulerian-Eulerian CFD Model for the Sedimentation of Spherical Particles in Suspension with High Particle Concentrations. *Engineering Applications of Computational Fluid Mechanics 4*, 116–126.

[5]   Berthier, J., and Brakke, K. A., *The physics of microdroplets*; John Wiley & Sons: Hoboken, New Jersey, 2012.

[6]   Bothamley, M. (2015). Gas/Liquid Separators: Quantifying Separation Performance. *Oil and Gas Facilities 2*, 21–29.

[7]   Bürkholz, A., *Droplet separation*; VCH Verlagsgesellschaft mbH: Weinheim, 1989.

[8]   Cadence CFD Solutions Y+ Boundary Layer Thickness, 2024.

[9]   Campbell, J. M., *Gas conditioning and processing: Volume 2: The equipment modules*, 7th ed.; Campbell Petroleum Series: Norman, Oklahoma, USA, 1992.

[10] Campbell, J. M. Gas-liquid separators sizing parameter, 2015.

[11] Che Sidik, N. A., Yusuf, S. N. A., Asako, Y., Mohamed, S. B., and Aziz Japa, W. M. A. (2020). A Short Review on RANS Turbulence Models. *CFD Letters 12*, 83–96.

[12]   Davidson, L. Fluid mechanics, turbulent flow and turbulence modeling, Göteborg, Sweden, 2012.

[13]   Davidson, L. An Introduction to Turbulence Models: Publication, Göteborg, Sweden, 2022.

[14]   Fabian, P., Cusack, R., Hennessey, P., and Neuman, M. (1993). Demystifying the selection of mist eliminators. *Chemical Engineering.*

[15]   Ferziger, J. H., and Perić, M., *Numerische Strömungsmechanik*; Springer: Berlin, 2008.

[16]   Firdani, T., Saputro, H., Muslim, R., Lasmini, S., and Khaniffudin In *ICST*, Institute of Electrical and Electronics Engineers: Piscataway, New Jersey, 2018.

[17]   Frey Marioni, Y., de Toledo Ortiz, E., Cassinelli, A., Montomoli, F., Adami, P., and Vazquez, R. (2021). A Machine Learning Approach to Improve Turbulence Modelling from DNS Data Using Neural Networks. *International Journal of Turbomachinery, Propulsion and Power 6*, 17.

[18]   Fröhlich, J., *Large-Eddy-Simulation turbulenter Strömungen: Mit 14 Tabellen*, 1. Aufl.; Lehrbuch : Maschinenbau; Teubner: Wiesbaden, 2006.

[19]   GEA Process Engineering Eindampftechnik mit mechanischer Brüdenverdichtung: Technologie und Anwendung, Ettlingen, Germany.

[20]   Hewitt, G. F., GAS-LIQUID FLOW In *A-to-Z Guide to Thermodynamics, Heat and Mass Transfer, and Fluids Engineering*; Begellhouse: 2006; Vol. G.

[21]   Holland, F. A., and Bragg, R., *Fluid flow for chemical engineers: F.A. Holland, R. Bragg*, 2nd ed.; Butterworth-Heinemann: Oxford, 1999.

[22]   Houben, J., Brunnmair, E., Weiss, C., and Pirker, S. (2016). CFD Simulations of Pressure Drop and Velocity Field in a Cyclone Separator with Central Vortex Stabilization Rod. *Journal of Applied Fluid Mechanics 9*, 487–499.

[23]   Hryb, D., Cardozo, M., Ferro, S., and Goldschmit, M. (2009). Particle transport in turbulent flow using both Lagrangian and Eulerian formulations. *International Communications in Heat and Mass Transfer 36*, 451–457.

[24]   Khoa, N. D., Kuga, K., Inthavong, K., and Ito, K. (2023). Coupled Eulerian Wall Film–Discrete Phase model for predicting respiratory droplet generation during a coughing event. *Physics of Fluids 35*, 1013.

[25] Koopman, H., *Analytical investigations concerning the performance of vane separators and experimental validation of droplet separation efficiency (KIT Scientific Reports ; 7690)*; KIT scientific reports, Vol. 7690; KIT Scientific Publishing: Karlsruhe, Baden, 2015.

[26] Lakehal, D. (2002). On the modelling of multiphase turbulent flows for environmental and hydrodynamic applications. *International Journal of Multiphase Flow 28*, 823–863.

[27] Laleh, A. P., and Svrcek, W. Y. (2012). Computational Fluid Dynamics-Based Study of an Oilfield Separator - Part I: A Realistic Simulation. *Society of Petroleum Engineers*, 57–68.

[28] Launder, B. E., and Spalding, D. B. (1974). The numerical computation of turbulent flows. *Computer Methods in Applied Mechanics and Engineering 3*, 269–289.

[29] Laurien, E., and Oertel, H., *Numerische Strömungsmechanik*; Vieweg+Teubner: Wiesbaden, 2011.

[30] Lecheler, S., *Numerische Strömungsberechnung: Schneller Einstieg in ANSYS CFX 18 durch einfache Beispiele / Stefan Lecheler*, Fourth edition; Springer Vieweg: Wiesbaden, 2017.

[31] Lesieur, M., and Métais, O. (1996). New Trends in Large-Eddy Simulations of Turbulence. *Annual Review of Fluid Mechanics 28*, 45–82.

[32] Liu, P., Ren, Y., Feng, M., Di Wang, and Hu, D. (2019). A performance analysis of inverse two-stage dynamic cyclone separator. *Powder Technology 351*, 28–37.

[33] Loth, E. (2000). Numerical approaches for motion of dispersed particles, droplets and bubbles. *Progress in Energy and Combustion Science 26*, 161–223.

[34] Luke, A., Tropfenabscheidung in technischen Apparaten In *VDI-Wärmeatlas*, Stephan, P., Kabelac, S., Kind, M., Mewes, D., and Schaber, K., Eds.; Springer Reference Technik, 2522-8196; Springer Vieweg: Berlin, Germany, 2019.

[35] Maliska, C. R., *Fundamentals of Computational Fluid Dynamics*; Springer International Publishing: Cham, 2023; Vol. 135.

[36] Manna, M. A Three Dimensional High Resolution Compressible Flow Solver, PhD. 1992.

[37] Menter, F. R. (1994). Two-equation eddy-viscosity turbulence models for engineering applications. *AIAA Journal 32*, 1598–1605.

[38] Muther, T. Simulation der mehrphasigen Strömung in einem Dampfzyklon mittels CFD, Masterthesis, Graz, 2018.

[39] Nitsche, M., *Kolonnen-Fibel: Für die Praxis im chemischen Anlagenbau*, Aufl. 2014; Springer Berlin Heidelberg: Berlin, Heidelberg, 2014.

[40] Pai, S.-I., and Oswatitsch, K., *Two-Phase Flows*; Vieweg+Teubner Verlag: Wiesbaden, 1977.

[41] Patil, A. V., Hofsteenge, J., Bujalski, J. M., and Johansen, S. T. (2022). DPM model segregation validation and scaling effect in a rotary drum. *Computational Particle Mechanics 9*, 693–707.

[42] Purnanto, M. H., Zarrouk, S. J., and Cater, J. E. In *34th New Zealand Geothermal Workshop*, 2012.

[43] Qaroot, Y. F., Kharoua, N., and Khezzar, L. In *Volume 7: Fluids Engineering Systems and Technologies*, American Society of Mechanical Engineers: 2014.

[44] Seon, G., Ahn, J., and Hwang, W. (2022). Analysis of the impact of flow characteristics on the separation efficiency and pressure drop of a cyclone-type oil separator. *Journal of Mechanical Science and Technology 36*, 273–283.

[45] Sheng, W. (2020). A revisit of Navier–Stokes equation. *European Journal of Mechanics - B/Fluids 80*, 60–71.

[46] Shoghl, S. N., Naderifar, A., Farhadi, F., and Pazuki, G. (2021). Optimization of separator internals design using CFD modeling in the Joule-Thomson process. *Journal of Natural Gas Science and Engineering 89*, 103889.

[47] Shukla, I., Tupkari, S. S., Raman, A. K., and Mullick, A. N. In AIP: 2012, pp 144–153.

[48] Sirignano, W. A., *Fluid dynamics and transport of droplets and sprays*, 2nd ed.; Cambridge University Press: Cambridge, 2010.

[49] Stenmark, E. On Multiphase Flow Models in ANSYS CFD Software, Masterthesis, 2013.

[50] Subramaniam, S. (2013). Lagrangian–Eulerian methods for multiphase flows. *Progress in Energy and Combustion Science 39*, 215–245.

[51] Utikar, R., Darmawan, N., Tade, M., Li, Q., Evans, G., Glenny, M., and Pareek, V., Hydrodynamic Simulation of Cyclone Separators In *Computational Fluid Dynamics*, Woo, H., Ed.; InTech: 2010, pp 241–266.

[52] Veress, Á., and Rohács, J., Application of Finite Volume Method in Fluid Dynamics and Inverse Design Based Optimization In *Finite Volume Method*, Petrova, R., Ed.; IntechOpen: 2012, pp 3–34.

[53] Verstappen, R., and Veldman, A. (1997). Direct numerical simulation of turbulence at lower costs. *Journal of Engineering Mathematics 32*, 143–159.

[54] Vesilind, P. A. (1980). The Rosin-Rammler particle size distribution. *Resource Recovery and Conservation*, 275–277.

[55] Yue, T., Chen, J., Wang, Y., Zhu, F., Li, X., Huang, S., Zheng, L., Deng, S., and Shang, Q. (2022). Numerical Analysis of Flow Characteristics of Upper Swirling Liquid Film Based on the Eulerian Wall Film Model. *Frontiers in Chemical Engineering 4*, 531.

[56] Zhang, J., Cai, R., and Shi, L. (2022). Hybrid RANS/LES/DNS of turbulence flow along a flat plate. *Journal of Physics: Conference Series 2248*, 012015.

[57] Zhiyin, Y. (2015). Large-eddy simulation: Past, present and the future. *Chinese Journal of Aeronautics 28*, 11–24.

[58] Ziebold, S. A. (2000). Demystifying Mist Eliminator Selection. *Chemical Engineering 107*, 94–100.

Appendix A

Simulation report

The simulation report of Variant a is presented. Variants b and c differ only in geometry/mesh, the setup is unchanged.

Ansys Fluent Simulation Report

Analyst	Jan Dudasko
Date	4/2/2024 12:01 PM
Company	TU Wien

Table of Contents

System Information

Application	Fluent
Settings	3d, double precision, pressure-based, SST k-omega
Version	23.2.0-10212
Source Revision	27b6146783
Build Time	May 29 2023 07:35:14 EDT
CPU	AMD EPYC 7302P 16-Core
OS	Linux

Geometry and Mesh

Mesh Size

Cells	Faces	Nodes
33716675	165375125	106431070

Mesh Quality

Name	Type	Min Orthogonal Quality	Max Aspect Ratio
fluid_volume	Poly Cell	0.11195275	36.831928

Orthogonal Quality
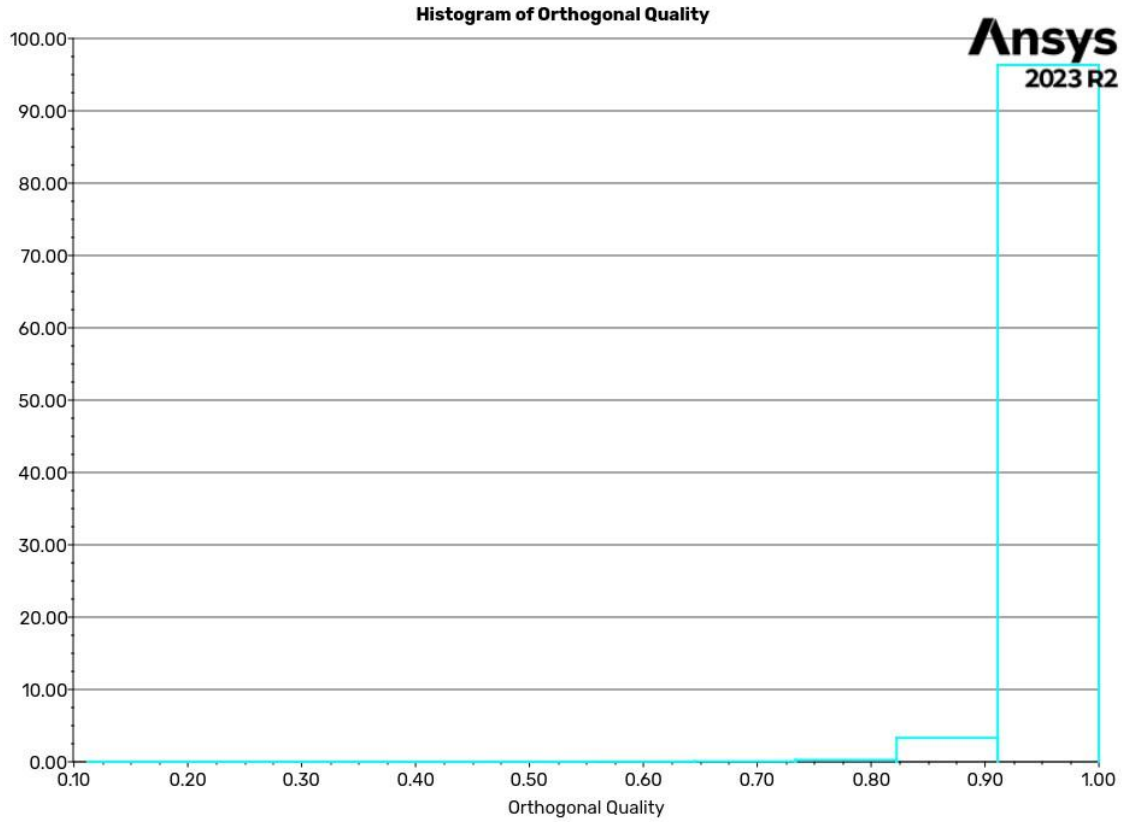
Simulation Setup

Physics

Models

Model	Settings
Space	3D
Time	Steady
Viscous	SST k-omega turbulence model
Heat Transfer	Enabled
Coupled Dispersed Phase	Enabled
Eulerian Wall Film	Enabled

Solver Settings

Equations	
Flow	True
Turbulence	True
Energy	True
Numerics	
Absolute Velocity Formulation	True
Under-Relaxation Factors	
Pressure	0.3
Density	1
Body Forces	1
Momentum	0.7
Turbulent Kinetic Energy	0.8
Specific Dissipation Rate	0.8
Turbulent Viscosity	1
Energy	1
Discrete Phase Sources	0.5
Pressure-Velocity Coupling	
Type	SIMPLEC
Skewness Correction	2
Discretization Scheme	
Pressure	Body Force Weighted
Momentum	Second Order Upwind
Turbulent Kinetic Energy	Second Order Upwind
Specific Dissipation Rate	Second Order Upwind
Energy	Second Order Upwind
Solution Limits	
Minimum Absolute Pressure [Pa]	1
Maximum Absolute Pressure [Pa]	5e+10
Minimum Static Temperature [C]	-272.15
Maximum Static Temperature [C]	4726.85
Minimum Turb. Kinetic Energy [m^2/s^2]	1e-14
Minimum Spec. Dissipation Rate [s^-1]	1e-20
Maximum Turb. Viscosity Ratio	100000

Solution Status

Iterations: 7000

	Value	Absolute Criteria	Convergence Status
continuity	0.005939653	0.006	Converged

59

Simulation report

	Value	Absolute Criteria	Convergence Status
x-velocity	3.454964e-07	0.001	Converged
y-velocity	3.44431e-07	0.001	Converged
z-velocity	1.278101e-07	0.001	Converged
energy	9.841622e-11	1e-06	Converged
k	1.427556e-05	0.001	Converged
omega	1.934941e-05	0.001	Converged

Plots

Residuals